



This work was accomplished in support of the Intelligence Advanced Research Projects Activity (IARPA), and produced for the U.S. Government under contract 2015-14120200002-002. The views and conclusions contained herein are those of the authors and should not be interpreted as necessarily representing the official policies or endorsements, expressed or implied, of IARPA or the U.S. Government or any of the authors host affiliations.

**Approved for Public Release;
Distribution Unlimited. Case
Number 17-1813**

© 2017 The MITRE Corporation.
All rights reserved.

McLean, VA

Variations in Infrared Spectroscopic Signatures

Overview of Underlying Physical Phenomenologies

*Christopher J. Deloye,
Richard S. Lepkowitz,
Michael S. West,
& Gary W. Euliss*

Sept 2015

This page intentionally left blank.

Executive Summary

This report summarizes the findings of a thorough literature search and elucidates key physical phenomena related to stand-off spectroscopy of low-abundance samples measured in realistic environments. The goal of this report is to assist key stakeholders of the Standoff Illuminator for Measuring Absorbance and Reflectance Infrared Light Signatures (SILMARILS) program in understanding the underlying phenomenology that can impact standoff spectral measurements.

The specific details of reflectance spectra depend on (1) intrinsic material physical properties that govern the light/matter interactions in that material and (2) extrinsic geometric properties of the material, its surroundings, and the illumination and viewing angles. Intrinsic effects explored within this report include material properties that are dependent on thermodynamic state and molecular level interactions (specifically those due to adsorption onto a substrate, varying degrees of hydration, and interactions within solutions). Important extrinsic factors identified in the literature review include particle size effects, optically thin material mixtures, sample morphology dependence, and illumination and viewing geometries. Key findings include:

- **Thermodynamic State:** When temperature or pressure variations result in either molecular conformational changes or phase changes, the shape and location of spectral features can change dramatically. For mixtures of reacting species, the temperature dependence of the reaction's equilibrium constant will lead to adsorption spectra variations driven by the mixture's changing composition. Materials with anharmonic intermolecular potentials experience shifts in spectral feature locations and changes in feature widths as temperature and pressure vary.
- **Molecular Level Interactions:** All forms of molecular level interactions introduce changes in the location and shape of a compound's spectral features. Additionally, the novel interactions provided by the secondary species (whether the substrate, solvent, or sorbed water molecules) can lead to the appearance of new spectral features or to the disappearance of some features due to bonding geometries. Relative concentrations of the participating species affect both the quantitative and qualitative nature of spectral feature variations.
- **Extrinsic Factors:** The scattering optical depth of a sample depends on the density and spatial-scale of inhomogeneities in the medium. The absorption optical depth depends on the total amount of the medium that light waves propagate through. Higher density, smaller-scale inhomogeneities tend to increase overall sample reflectance, while the corresponding change in spectral feature depth and width depends on whether the material is optically thick or thin on the spatial scale set by the inverse of the inhomogeneity density. Non-monotonic feature depth/width changes can occur as the inhomogeneity density varies monotonically. For mixtures involving optically thin component media, the mixture spectrum typically evolves non-linearly between the pure component spectra as a function of mixture composition and it is not uncommon for the mixture spectrum to not be bounded by the component spectra over at least some wavelength range. Variations in spectral contrast and overall spectral shape typically are present as illumination and viewing angles change.

Finally, we review the existing literature on spectral signatures of specific compounds of particular concern from a security-related perspective.

Table of Contents

1	Introduction	1
2	Spectral Variations due to Extrinsic Factors in One-Dimensional Planar Geometry	3
3	Spectral Signature Variations: Examples	7
3.1	Intrinsic Factors	7
3.1.1	Thermodynamic State	8
3.1.2	Molecular Level Interactions	11
3.1.2.1	Adsorption	11
3.1.2.2	Hydration	14
3.1.2.3	Interactions in Liquid Solutions	18
3.2	Extrinsic Factors	20
3.2.1	Particle Size Effects	20
3.2.2	Optically Thin Samples in Mixtures	21
3.2.3	Other Sample Morphology Effects	23
3.2.4	Illumination and Viewing Angles: Sample BRDF	24
4	Spectral Signatures of Example Explosive and Chemical Warfare Agent Related Com- pounds	25
Appendix A	Planar Slab Reflectance: Definitions, Notation, and Derivation	31

1 Introduction

In remote sensing applications, the infrared (IR) spectroscopic identification of a given molecular compound typically relies on matching the measured spectrum of some unknown substance against pre-measured template signatures of known materials. Usually, the number of such template signatures used for a given compound is relatively small and represent measurements on a limited number of compound samples under a limited set of conditions, which may or may not be well controlled or characterized. This presents a potential problem: the spectral signatures of a given substance depends on a myriad of factors, and having only a limited number of template spectra, especially over a limited or unknown range of salient parameters, could lead to mischaracterization or even missed detections of a material of interest.

The degree to which spectral signatures can vary depends on the nature of the sample under consideration. For example, in the case of macroscopic solid or liquid samples that are optically thick or in the case of non-interacting gas phase samples under standard conditions, a limited number of template spectra taken on similar samples may provide “close-enough” examples to allow detection over a wide range of conditions encountered *in situ*. (Accurate quantitative analysis and characterization of *in situ* samples based on limited sets of experimental reference spectra is likely another story, however.) On the other hand, when the sample quantity is small or the material exists in a form that is optically thin (i.e., translucent or transparent) or experiences molecular-level interaction with its surroundings, a wider range of spectral variations is likely to occur.

In the context of detecting and identifying trace and residue amounts of compounds of interest, it is this latter case that is most relevant. Complicating matters here is the fact that some of the causes of spectral variation in the low-abundance limit can depend on a sample’s surroundings. In such cases, detection via simple template matching may be woefully insufficient, particularly when interactions between a sample and its surroundings induce shifts in the wavelength location of the sample’s characteristic spectral features. Spectroscopic detection of trace quantities can therefore be expected to be a challenging endeavor due not only to the limited signal afforded by the small amounts of target analyte present but also on the wider spectral variability that can be exhibited by trace samples. The main goal of this report is to provide an overview of various physical mechanisms that can produce such spectral signature variations, paying specific attention to mechanisms that may be of particular import to signature variations in the trace quantity limit.

Because spectral signatures are determined by light/matter interactions that depend on both molecular properties and bulk-sample geometric factors, factors influencing spectral variations can be either intrinsic or extrinsic in nature. Intrinsic factors are those that influence how light fundamentally interacts with a given substance. This interaction is quantitatively described by the medium’s complex refractive indices (or, optical constants), $\tilde{n} = n + i\kappa$. The real part, n , of the refractive indices describe an electromagnetic (EM) wave’s phase velocity in the medium while the imaginary part, κ , is related to the wave’s in-medium amplitude attenuation rate. The \tilde{n} are wavelength (λ) dependent quantities and are explicitly related to a medium’s quantum mechanical energy eigenstates and to the rate at which transitions between these states occur [1]. As such, \tilde{n} will depend not only on a substance’s molecular composition but also on its molecular geometry. So, e.g., \tilde{n} differs between solid, liquid, and gas phases [e.g., 2, 3] and between different molecular configuration states within a given phase [e.g., 4, 5]. Chemical or physical interactions between a molecule and its surroundings alter the quantum states of the interacting media and, hence, their respective \tilde{n} .

The primary extrinsic factors of relevance are the geometry of both the target sample and its surroundings: EM waves scatter due to inhomogeneities in \tilde{n} [6]. Such inhomogeneities can be due to interfaces between two distinct media, fluctuations in a medium’s density, microscopic compositional variations, defects in a solid’s crystal lattice, amongst other causes. The specifics of a medium’s geometry as it determines and relates to \tilde{n} heterogeneities plays a significant role in setting the magnitude and spatial distribution of the scattered EM fields. Factors such as particle size and shape, internal inhomogeneities, etc. can all play a significant role in a medium’s spectral signature. The spatial distribution of the scattered fields, in turn, determine a medium’s bidirectional reflectance distribution function (BRDF), which is of importance in reflectance and emittance spectrometry[e.g., 7]. When the target sample is optically thin, its surroundings can significantly influence its spectral signature with the spectra of such optically-thin “mixtures” depending on the relative values of the components’ \tilde{n} and the overall geometry.

For a trace quantity sample, the likelihood of it experiencing significant interactions with its surroundings (altering its \tilde{n}) while also existing in an optically-thin morphological state (increasing the importance of the surrounding’s properties on the resulting scattering) increases. As such, the impact of both intrinsic and extrinsic factors on the spectra of low-abundance samples can be particularly significant. In the following, we will provide specific examples of how both types of factors alter a medium’s spectral signature while also highlighting general trends that occur across these examples. Throughout our emphasis will be on providing a qualitative understanding of the physics underlying the observed phenomenology. The remainder of this report is organized as follows. In §2 we examine the simple, idealized case of one-dimensional planar media. We do so for two reasons. One, to demonstrate that even in this simple geometry—and only considering the impact of *extrinsic* factors—there is already a rich phenomenology of spectral signature variation. Two, to illustrate general principles that connect extrinsic media properties to spectral signature variations. These general principles will continue to hold in the case of more complex sample geometries. We then turn to consideration of these more complex sample geometries and their spectral signature phenomenology in §3 by highlighting examples from the literature that illustrate how various factors (both intrinsic and extrinsic) can impact the observed spectra in various material phases. In §4, we provide summaries of the literature regarding the spectral signatures of some compounds of specific security-related concern and the variations in these signatures that have been documented.

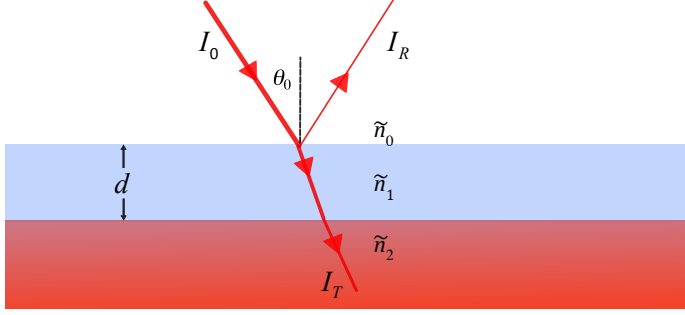


Figure 1: Basic planar slab media geometry utilized to demonstrate spectral signature variations with extrinsic factors.

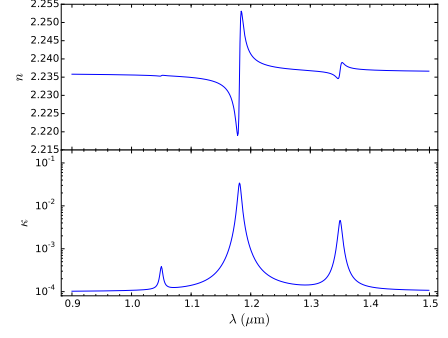


Figure 2: The set of refractive indices used for medium-1 in the calculation of planar slab reflectances.

2 Spectral Variations due to Extrinsic Factors in One-Dimensional Planar Geometry

Many of the spectral signature variation trends produced by extrinsic factors can be seen even in the simple case of infinite planar media. The geometry of this idealized case is shown in Figure 1 (see also Figure A-1 for further details). Media heterogeneities in this geometry occur only in the vertical direction and consist of interfaces between otherwise homogeneous layers with individually specified thicknesses; each layer is infinite in extent in the horizontal plane across and out of the page. Further, the stack of media layers is restricted to the lower half of the vertical plane. Incident light originates from the upper-half plane, which is filled with an incident medium with optical constants $\tilde{n}_0 = 1$ (i.e. air). For simplicity, we will consider plane-wave incident radiation with a specified medium-0 wavelength of λ_0 and whose propagation direction makes an angle θ_0 with the media stack's surface normal. In this section, we will utilize this geometry to highlight the general principles that determine how extrinsic factors affect the qualitative nature of a medium's spectral signatures. These general principles will continue to be applicable in more complex, realistic sample geometries.

Here we will focus on a sample's spectral reflectance, $R \equiv I_R/I_0$ where I_0, I_R are the incident and reflected EM-waves' spectral energy flux components normal to the interface (dimensions of [energy area⁻¹ time⁻¹ wavelength⁻¹]; note also that there is an implicit λ -dependence on all these quantities). To start, we will first examine the simplest case of a single layer of a homogeneous medium with some finite thickness, d , on top of an infinitely thick substrate (i.e. the exact case shown in Figure 1). The layer and substrate have λ -dependent optical constants \tilde{n}_1 and \tilde{n}_2 , respectively. For simplicity, we will only consider the case of incoherent reflection¹. The sample's incoherent R in this particular case (see Appendix A for details) is given by:

$$R = \frac{R_{01} + R_{12}e^{-2\alpha d} (T_{01}T_{10} - R_{01}^2)}{1 - R_{01}R_{12}e^{-2\alpha d}}. \quad (1)$$

¹ When d is such that an EM-wave packet's phase coherence can be maintained across the layer, coherent interference occurs between transmitted and reflected waves within the sample layer, altering the overall reflectance.

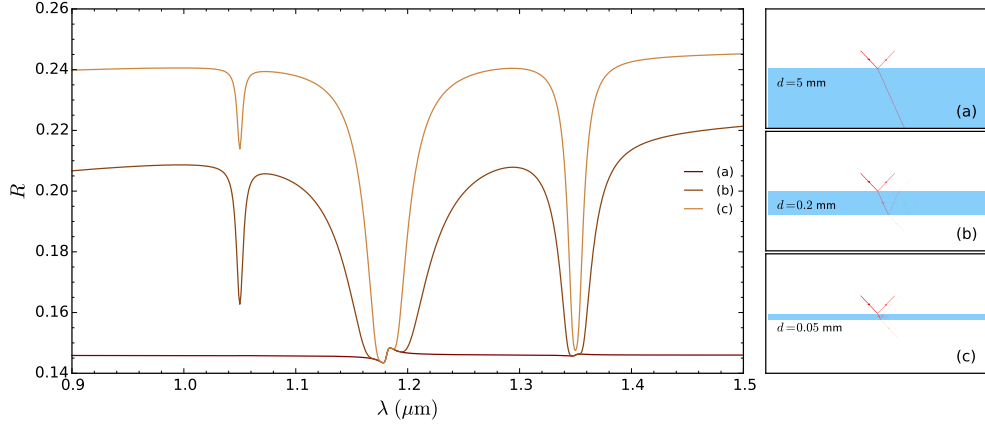


Figure 3: Reflectance of a planar slab as a function of slab thickness.

The R_{jk} and T_{jk} are the single-interface flux reflectance and transmittance coefficients at the boundary between incident medium j and transmitting medium k . Both are θ_0 -dependent quantities. At normal incidence ($\theta_0 = 0$), these coefficients are given by:

$$R_{jk} = \left| \frac{\tilde{n}_j - \tilde{n}_k}{\tilde{n}_j + \tilde{n}_k} \right|^2, \quad T_{jk} = \frac{n_k}{n_j} \left| \frac{2\tilde{n}_j}{\tilde{n}_j + \tilde{n}_k} \right|^2. \quad (2)$$

The attenuation coefficient α determines the attenuation rate suffered by an EM-wave per perpendicular distance it travels in medium-1 and is primarily determined by κ_1 . The attenuation coefficient is also θ_0 -dependent, but at normal incidence $\alpha = 4\pi\kappa_i/\lambda_0$.

From these expressions we can highlight several basic principles. The reflectance of an EM-wave only occurs at boundaries where $\tilde{n}_j \neq \tilde{n}_k$, with R increasing for greater differences between the optical constants. This is essentially just the statement in this particular geometry of the general principle that scattering occurs due to inhomogeneities in \tilde{n} . Within each homogeneous region, scattering does not occur, but the wave experiences attenuation when $\alpha \neq 0$. Additionally, R has an explicit dependence on R_{12} ; put another way, the overall reflectance of a sample *depends* on its surroundings, not just on properties of the sample². The extent to which the surroundings end up influencing R will depend on the specific geometry and \tilde{n} -values involved. Note also that even if R_{12} were not influenced by a change in adjacent media, the overall R even in this simple geometry is neither an additive or multiplicative function of the individual component reflectances.

For specificity, we will illustrate how R changes under various specified geometries by taking \tilde{n}_1 equal to the set of optical constants shown in Figure 2. This particular set of \tilde{n} is synthesized from the sum of three Lorentzian resonances whose central λ -values occur in the wavelength range shown plus a background dielectric constant specified so that n differs significantly from unity. To start, we consider R in the case medium-1 is surrounded on both sides by air (i.e., $\tilde{n}_0 = \tilde{n}_2 = 1$). Figure 3 provides examples of how R changes with d for this particular set of \tilde{n} . Case (a) in Figure 3 illustrates R when d is such that $\alpha d \gg 1$. In this case medium-1 is optically thick, meaning that light waves are attenuated essentially to zero amplitude before encountering a second interface. The only scattering occurs at the media $0 \rightarrow 1$ interface and the resulting $R = R_{01}$ (as can be seen

² This is a basic property of the the EM-scattering problem in general: the governing Maxwell Equations are partial differential equations whose solutions are conditioned on specification of boundary conditions.

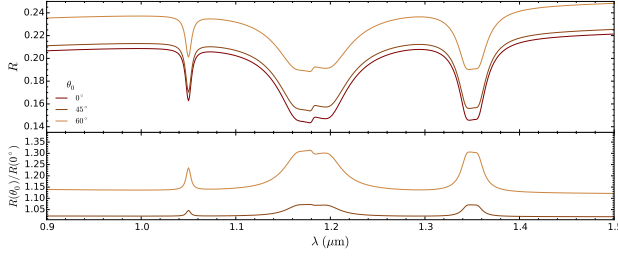


Figure 4: Reflectance of a planar slab at various illumination angles.

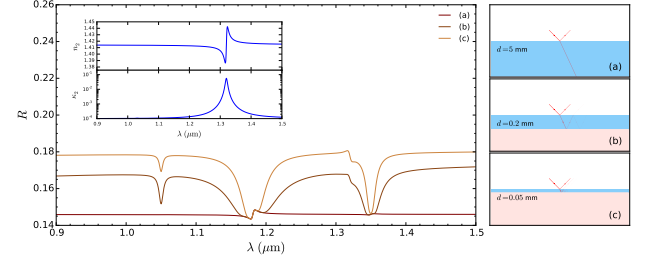


Figure 5: Impact of changing the refractive indices of medium-2 on the reflectance of the planar slab sample.

by taking $\alpha d \rightarrow \infty$ in Equation 1). In our particular case, $n_1 \gg \kappa_1$ so the spectral character of R_{01} essentially mirrors that of n_1 which does not vary strongly with λ . Because of this, R is essentially constant in case (a) and certainly does not exhibit any indication of typical spectral absorption features. We should note that there are cases where $\kappa \gtrsim n$ [e.g., 8–10]; in such cases the first-interface reflection coefficient can exhibit more spectral contrast since κ varies much more rapidly than n with λ .

Cases (b) and (c) illustrate the behavior of R when a second interface is present at an optical-depth $\alpha d \lesssim 1$. Scattering off the second interface produces additional reflected flux, increasing R . Most of the λ -range considered here is in this regime for the d -values specified. However, around the central λ of the strong feature near $1.18 \mu\text{m}$, medium-1 remains optically thick even for case (c) ($d = 0.05 \text{ mm}$). Apart from the increased R , the other qualitative difference between these and case (a) is the appearance of more typical absorption features in the R spectra. These features result from the differential attenuation experienced at differing λ as the wave propagates through medium-1 and scatters back off the second interface. The width and depth of absorption features narrow and decrease, respectively, as the layer's d decreases. However, as R_{12} and R_{10} do not depend on d , the overall increase in R with d between cases (b) and (c) results from the decrease in absorption occurring in the wings of the resonances as d decreases.

Variations of R with respect to incidence angle, θ_0 , also occur in this planar geometry. (Given the idealized, purely specular nature of the scattering surfaces, the view-angle dependence is a delta-function of the incidence angle; i.e., $R \neq 0$ only at a view-angle of θ_0). The upper panel of Figure 4 shows the polarization-averaged R at several different θ_0 for a slab thickness of $d = 0.02 \text{ mm}$. The $\theta_0 = 0^\circ$ case here is the same as case (b) in Figure 3. The increase in reflectance at 45° and 60° over that at $\theta_0 = 0^\circ$ is characteristic of R behavior in this planar interface geometry. Note, further, that there is a spectral dependence in the relative increases of R . Specifically, R within absorption bands increases more rapidly than in the continuum regions, as highlighted in the lower panel of Figure 4. This results in a decrease in band depth at these θ_0 and a reduction in spectral contrast. More generally, this example shows that one should not expect a sample's spectrum to maintain a fixed relative shape at varying illumination and view angles.

Figure 5 demonstrates one way in which a sample's surroundings can alter its light-scattering properties: via changes in surrounding media optical properties. Specifically, Figure 5 shows the impact of changing the optical constants of the substrate from $\bar{n}_2 = 1$ to the set shown in Figure 5's inset. The three cases shown in Figure 5 correspond to the cases shown in Figure 3. In case (a), medium-1 is still optically thick and the underlying substrate makes no difference to

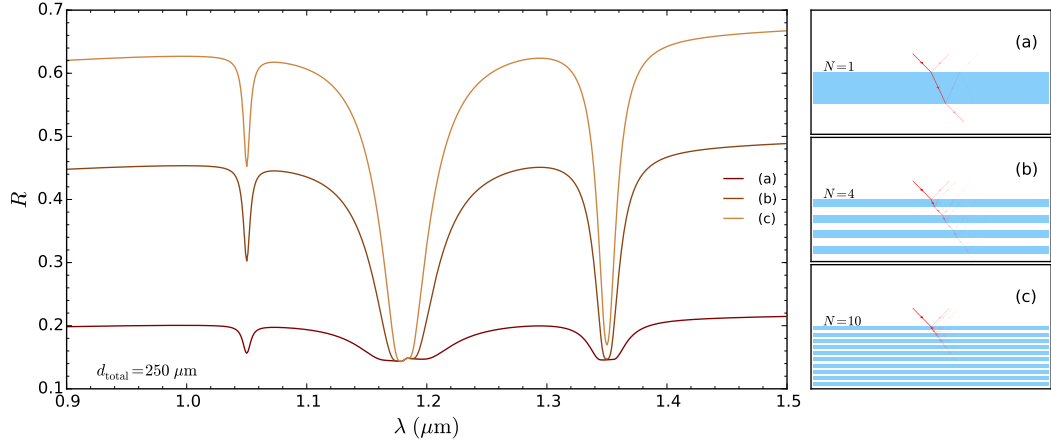


Figure 6: Impact of varying the number and thickness of multiple planar slabs on reflectance. Here, as the number of medium-1 slabs increase, the individual slabs thicknesses decrease to maintain a constant total thickness of medium-1 present.

the scattering properties. The case (a) R in both Figures is therefore the same. At lower optical depth, the substrate's properties begin to have an impact and the case (b) and (c) reflectances are altered. The mismatch between \tilde{n}_1 and \tilde{n}_2 in Figure 5 is less than in Figure 3, *reducing* the single-interface reflectance, R_{12} , at the bottom of medium-1. This in turn reduces R overall per equation (1) and as seen in comparing Figure 5 to Figure 3. Another qualitative difference appears in Figure 5 in the altered shape of the $\lambda = 1.35 \mu\text{m}$ band. The new \tilde{n}_2 has an absorption feature that partially overlaps this \tilde{n}_1 band, producing the notched morphology in the combined band. While this particular example was intentionally contrived, it still illustrates the point that when a sample's surroundings have optical constants that are similar to the sample's or that change rapidly over λ -ranges where the sample's diagnostic features occur, the potential for significant changes in the feature's appearance and strength will be present.

Finally, we consider a slight modification to the planar sample geometry and consider multiple interfaces. Figure 6 examines the reflectance of three different cases where stacks of medium-1 slabs are surrounded and interspersed with layers of air. The three cases differ in the number, N , of medium-1 slabs present. However, the summed thickness of all the medium-1 slabs is the same in each case (i.e., the total amount of medium-1 present is constant). For $N > 1$, R is calculated using the so-called transfer-matrix method that generalizes the calculations of R and T to the multi-slab case [see, e.g., 11]. As N increases, the individual slab thickness decreases, altering the relative importance of scattering and absorption in each layer: scattering occurs at each media interface while the single-slab absorption decreases with d . The net effect is for R to increase overall with increasing N even within absorption features at λ -values where individual slabs are not optically thick. In such a regime, R increases rapidly with N as seen in Figure 6. While the absolute R level of absorption features increases with N , the relative depth and width of features vary in a more complicated manner. For the cases considered in Figure 6, the relative depth of each feature increases with N and there is a narrowing of each feature in the $N = 10$ case. However, for even larger N , a *decrease* in both width and depth of the features would be observed as scattering becomes increasingly dominant. The overall increase in R and varying feature morphology seen here carries over into more realistic cases with analogous phenomenology observed as a function of particle-size in particulate media, for example.

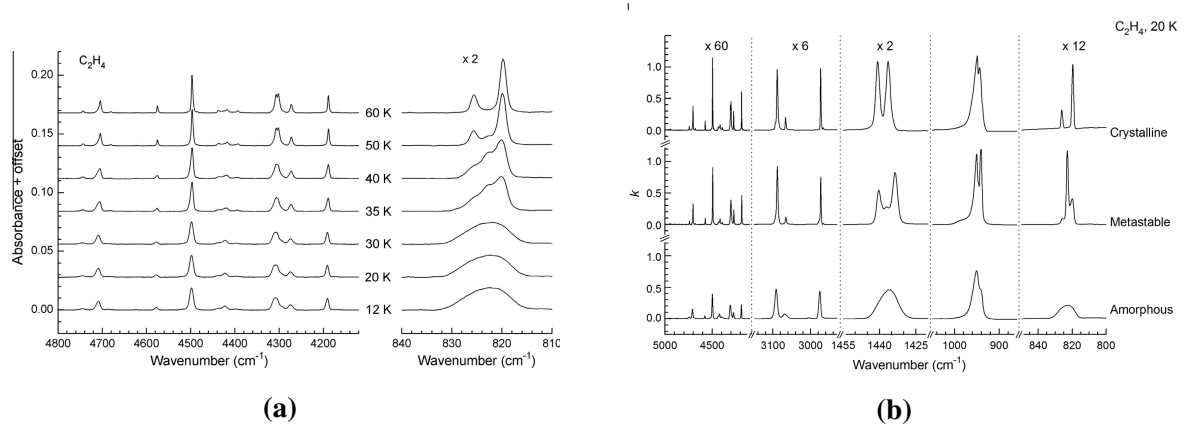


Figure 7: (a) Temperature evolution of amorphous ethylene (C_2H_4) ice formed at 12 K and warmed. A phase transition to the crystalline solid conformation occurs around 45 K. (b) C_2H_4 ice absorbance as a function of solid configuration at 20 K. Reproduced from Figures 5 and 8 of [12].

3 Spectral Signature Variations: Examples

Our discussion in §1 highlighted the generic physics that underpin the two categorical sources of spectral signature variations: variations in a material's properties that change \tilde{n} and variations in the geometry of the material sample and its surroundings that alter the overall scattering characteristics. Variations in \tilde{n} are due fundamentally to changes in the quantum mechanical states available in a medium and the states' respective occupation numbers. Variations due to geometric factors fundamentally result from the fact such changes alter the boundary conditions of the EM-wave scattering problem. We also have just seen in §2 that significant variations in spectral signatures can be produced just by solely changing geometric factors in the simplest case of one-dimensional planar media. With this general foundation in place, in this section we will discuss examples of how specific changes in a medium's intrinsic and extrinsic properties lead to spectral signature variations, focusing particularly on factors that can be expected to have significant influence on the spectral variations in trace-quantity samples.

3.1 Intrinsic Factors

As already discussed, a material's refractive indices are directly tied to its spectrum of quantum states and their occupation numbers. Multiple factors influence the exact energy levels available while its temperature typically controls the occupation numbers of these available states. From this point of view, intrinsic factors influencing a material's spectral signatures are those factors that alter a substance's \tilde{n} via changes in its quantum mechanical state. Such factors include the thermodynamic state of a material and interactions with its surrounding environment that lead to changes in the states available to the overall system, whether by altering existing states or creating new states that come about due to such interactions.

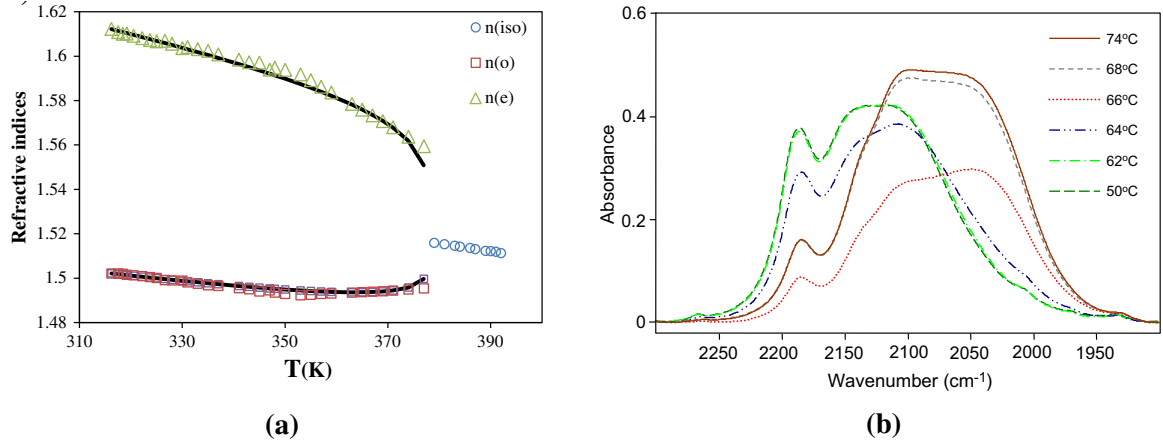


Figure 8: Temperature driven conformational changes and \tilde{n} in liquid crystals. (a) shows the evolution of ordinary and extraordinary n in the liquid crystal C_7-B-C_5 (λ -value was unspecified); increasing T_{th} decreases crystal ordering, reducing the degree of birefringence. At $T_{\text{th}} \approx 380$ K, a phase change to the isotropic state occurs. (b) Evolution of absorbance spectra of the liquid crystal 7TPB near $\nu \approx 2100 \text{ cm}^{-1}$. The blue-shift and evolution in the relative strength of the two features accompanies a change from crystalline to isotropic phase. Reproduced from Figure 1 of [5] and Figure 7 of [20], respectively.

3.1.1 Thermodynamic State

A material's temperature, T_{th} , and density, ρ (or, alternatively, pressure, P) influences \tilde{n} values in several ways. Variations in temperature play both direct and indirect roles in modifying \tilde{n} . Changes in T_{th} alter the occupation numbers in various quantum mechanical states, with corresponding changes in \tilde{n} [13, 14]. On the other hand, T_{th} indirectly affects \tilde{n} via molecular conformation and phase changes in pure materials [5, 12, 15–24] and via its influence on the equilibrium constants for reacting materials [25, 26]. Varying P will alter a medium's density and, hence, the medium's mean intermolecular distances. For materials with anharmonic intermolecular interaction potentials, such changes in mean separation lead to shifts in their states' energy levels, with corresponding shifts in the λ (or alternatively, the wavenumber, ν) at which spectral resonances occur [27, 28]. Phase changes can also be driven by P -induced ρ variations [29–32]. In some cases, the induced phases can persist even after a return to the original pressure [33–35], a phenomenon of potential relevance to spectroscopic indications of shock-wave compressed media. Since ρ also typically varies with temperature, T_{th} variations will indirectly induce ρ -dependent \tilde{n} variations [e.g., 36, 37]. In liquids and solids, these indirect effects appear to be the dominant mode through which T_{th} -variations impact a material's spectral character.

Temperature dependent conformational changes occur in numerous contexts. For example, Hudson et al. [12, 38] considers the \tilde{n} behavior of ethane (C_2H_6), ethylene (C_2H_4), and acetylene (C_2H_2) ices, each of which occur in several T_{th} -dependent solid phases. Incidentally, C_2H_6 and C_2H_4 provide examples of compounds with T_{th} -dependent irreversible phase changes where the lower- T_{th} amorphous and metastable phases convert to a higher- T_{th} crystalline phase. This higher- T_{th} phase however does not revert to the other phases when cooled [12]. Figure 7a shows this impact on the absorbance of warming C_2H_4 ice formed at 12 K through this phase transition. Note also that the C_2H_4 amorphous phase exhibits T_{th} -dependent absorption feature structure even be-

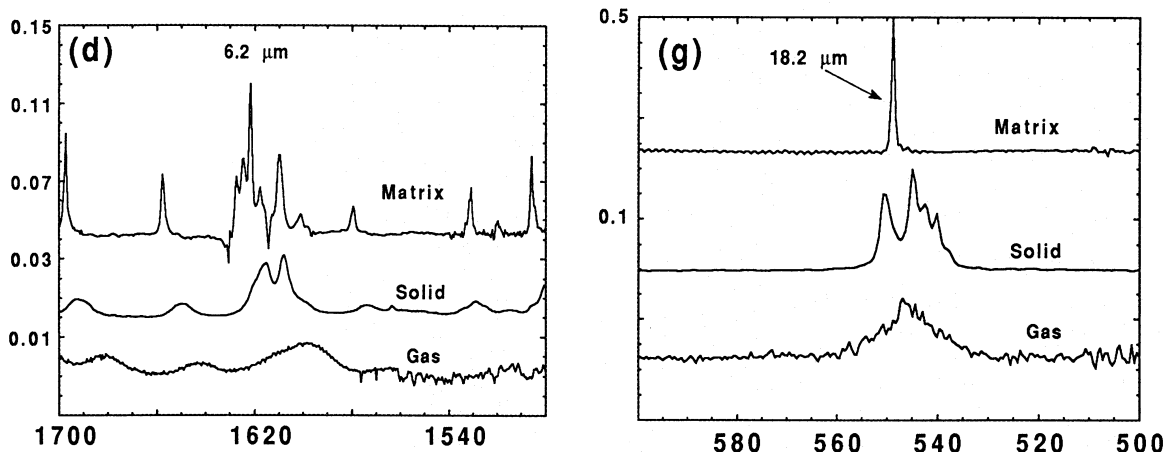


Figure 9: Comparison between the absorbance of solid ($T_{\text{th}} = 300$ K) and gaseous ($T_{\text{th}} = 770$ K) forms of $\text{C}_{24}\text{H}_{12}$ in two selected ν -ranges. Peak narrowing and shifting to higher ν between the gas and solid states is apparent as is the appearance of new features. The y-axis shows absorbance (arbitrary units with offsets between plot lines); the x-axis, ν in cm^{-1} . Reproduced from Figure 2 of [15].

fore the phase transition is reached. Figure 7b shows that the three solid C_2H_4 conformations (all at $T_{\text{th}} = 20$ K) exhibit significant differences in the imaginary part of their optical constants, κ . Another example of T_{th} -driven conformation changes is provided by Zakerhamidi and Rahimzadeh [5] [see also 24] in a study of several cyano-benzoate liquid crystals. In the crystalline phase, these materials are birefringent with the values of the ordinary and extraordinary real-part of the optical constants, n , dependent on the degree to which the individual molecules are aligned, which in turn is T_{th} -dependent. Figure 8a shows the evolution of the two n values as T_{th} varies for one of these compounds. The n -evolution is smooth up to $T_{\text{th}} \approx 380$ K at which point a phase transition to an isotropic state occurs and the material's birefringence disappears. Majewska et al. [20] provides a further example of a liquid crystal phase change in terms of κ : Figure 8b shows a dramatic shift in an absorption feature's ν -location as the material transitions from an isotropic to crystalline state.

Joblin et al. [15] measured the absorbance of solid and gaseous forms of several polycyclic aromatic hydrocarbons (PAHs). Figure 9 shows their reported differences in the absorption spectra of coronene ($\text{C}_{24}\text{H}_{12}$) in two ν -regions. The solid phase spectra show the clear appearance of new absorption features combined with ν -shifts in features present in the gas phase. On the other hand, Boer et al. [25] provides an example of T_{th} induced \tilde{n} changes in chemically-interacting mixtures of aqueous solutions of common atmospheric aerosols. Specifically, aqueous solutions containing both

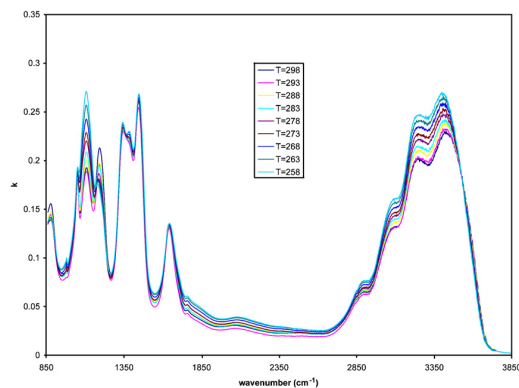


Figure 10: κ vs. ν for an aqueous solution of ammonium sulfate and sulfuric acid. The SO_4^{2-} and HSO_4^- ions concentrations are T_{th} -dependent, producing the change in the relative strengths of the sulfate ion band at $\nu \approx 1100$ cm^{-1} and the bisulfate bands at $\nu \approx 880$, 1050 , and 1190 cm^{-1} . Reproduced from Figure 9 of Boer et al. [25].

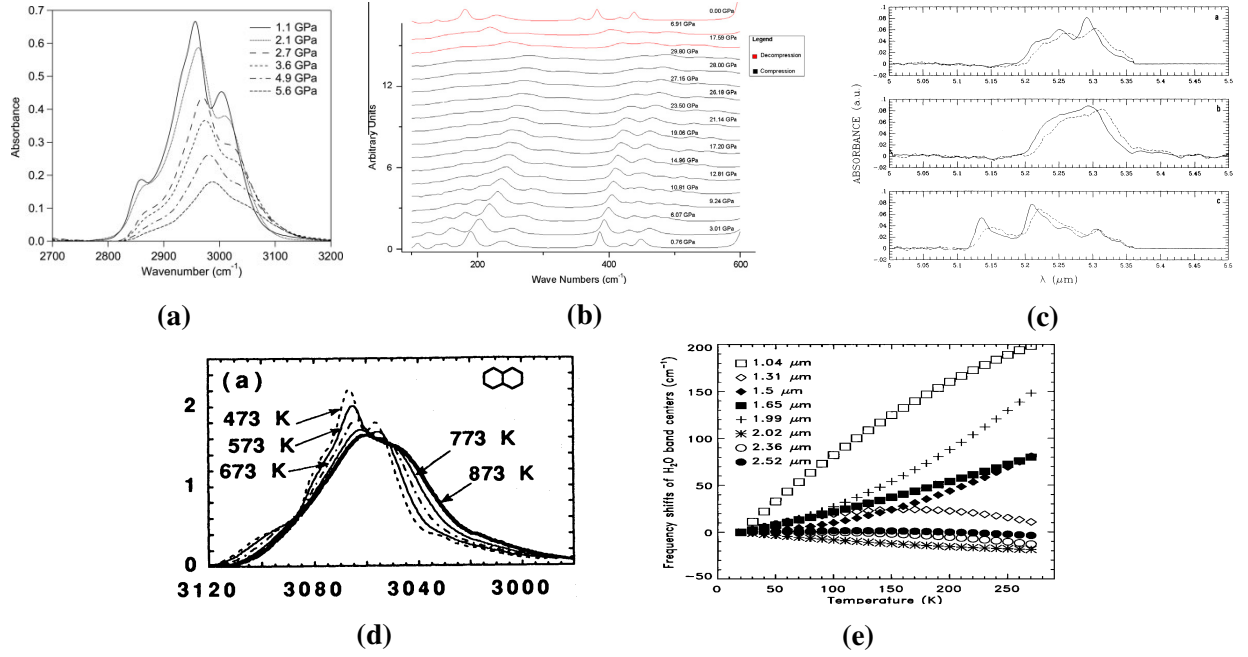


Figure 11: Anharmonic potential effects under changing P and T_{th} . (a) C-H band absorption spectra of poly(methyl methacrylate) morphology changes with P ; reproduced from [28]. (b) HMX absorption spectra changes with P ; reproduced from [32]. Solid (c) and gas (d) phase PAH molecules absorption band morphology changes with T_{th} ; reproduced from [36, 40]. For (c), $T_{th} = 303$ K for the solid lines and 513 K for the dashed lines. (e) Observed shifts in H₂O ice NIR bands with T_{th} , demonstrating that band shift behavior differing from the typical discussed here can occur; reproduced from [18].

ammonium sulfate and sulfuric acid show significant variations in the magnitude of κ within certain bands. The reason for this is that the equilibrium constant of the sulfate-bisulfate ion reaction ($\text{SO}_4^{2-} \rightleftharpoons \text{HSO}_4^-$) in aqueous solution is T_{th} -dependent [39]. As the equilibrium concentration of these two ions changes, the absorption in their respective bands vary significantly (Figure 10).

Both T_{th} and P variations alter \tilde{n} in materials with anharmonic intermolecular potentials. Under increases in pressure (increasing ρ), absorption features typically broaden and shift to higher ν (corresponding to energy levels shifting upward). This behavior is observed in Figures 11a and 11b, which shows the absorbance in the C-H stretching modes of poly(methyl methacrylate) and in the far-infrared absorbance spectra of octahydro-1,3,5,7-tetranitro-1,3,5,7-tetrazocine (HMX) evolving under increasing P [28, 32]. On the other hand, at (nearly) constant P , increasing T_{th} tends to decrease ρ , shifting feature to lower ν (larger λ) as occurs with decreasing P . Figures 11c and 11d show examples of this behavior in the case of different PAH molecules in the solid [40] and gas phases [36], respectively. However, the analogy here between an increasing T_{th} and decreasing P is not complete: feature widths broaden with increasing T_{th} in these examples, not narrow as with decreasing P . This difference in behavior is likely explained by the fact that with increasing T_{th} , while the material's quantum energy levels shift downward, there is an overall shift in state occupation number toward higher-level states. Apparently in these examples, the corresponding increase in sample's translation/vibrational kinetic energy produces observable increases in feature Doppler broadening. Finally, we note that while these absorption feature morphology trends with P and T_{th} are typical, they are not ubiquitous. Figure 11e shows the T_{th} shifts seen in near-infrared (NIR) bands of H₂O ice, several of which shift to higher ν with increasing T_{th} [18].

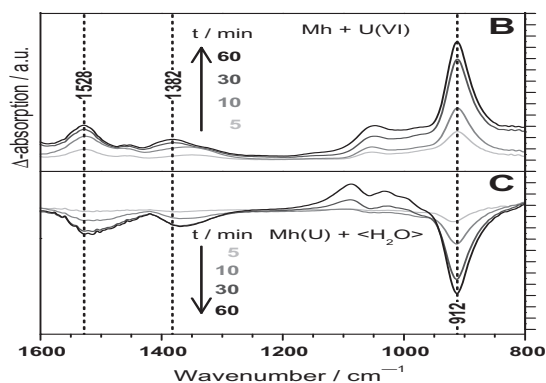


Figure 12: Time-resolved difference spectra of U(VI) adsorption and desorption on maghemite. Shifts and width changes in the 1526 and 1382 cm^{-1} bands can be seen as the U(VI) concentration changes. Reproduced from Figure 1 of [41].

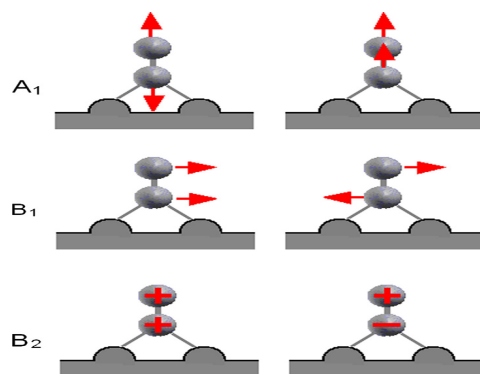


Figure 13: Vibration modes of a diatomic molecule absorbed in a bridge geometry. Only the modes with dipole moments components perpendicular to the substrate surface (A modes here) are IR active. Reproduced from Figure 12 of [37].

3.1.2 Molecular Level Interactions

Atomic and molecular level interactions between a substance and its environment often alter the quantum states available to the system as a whole. Here we will focus on three particular contexts in which molecular-level interactions can have significant impact on a substance's spectral signature: adsorption onto substrate interfaces, interactions of H_2O molecules with solids, and solute/solvent interactions.

3.1.2.1 Adsorption

Adsorption denotes the phenomenon of atoms or molecules of one substance (adsorbate) bonding to the surface of another substance (substrate or adsorbent). The impact of this process on the refractive indices of the participating substances depends on multiple factors including the nature of these interactions, the particular siting and bonding geometry of the adsorbate with the substrate, and adsorbate concentration, amongst others. In particular, adsorbate bonding modes can be highly anharmonic [37] and show T_{th} -dependent frequencies and structures [37, 42]. For reviews on specific aspects of adsorption phenomenology see [43] and [37].

Adsorbate/substrate interactions can modify adsorbate band shape and location (Figure 12). To give some sense of the range of examples, absorption feature shifts have been reported in the case of the nucleobases adenine and uracil adsorbed on fosterite [44], UO_2 on ferrihydrite and U(VI) on maghemite [41, 45], and *tert*-butyl halides on faujasite [46]. Feature shifts and broadening are also seen in 2-amino-6-methylbenzothiazole on a colloidal silver substrate [47] and for numerous molecular gases [48, and references therein]. Bands present in a molecule's free-state may even disappear upon adsorption depending on the adsorbate's bonding geometry. Band visibility is controlled by so-called surface selection rules [49, 50]: only modes that produce adsorbate vibrations with components perpendicular to the surface will be visible (Figure 13). Yamada et al. [51] discusses how this phenomenology can be used to determine the orientation of nucleobases on a

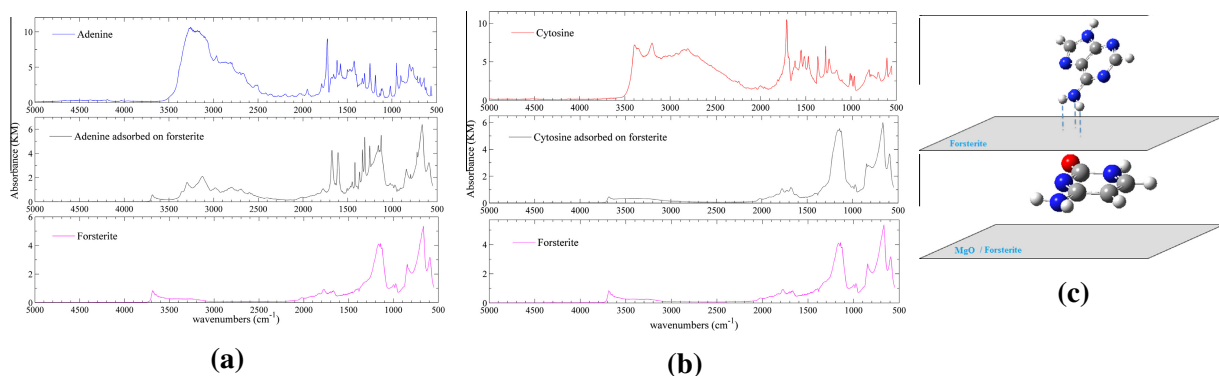


Figure 14: (a) and (b): Infrared absorbance spectra of adenine and cytosine adsorbed on forsterite. Top plot provides pure material spectra while the middle panel shows each adsorbate on the substrate. Adenine modes are still present when adsorbed while cytosine modes disappear. (c): The orientation of adenine (top panel) and cytosine (bottom panel) when adsorbed onto the substrate inferred from their IR mode activity. All figures reproduced from [44].

copper substrate. Similarly, the disappearance of characteristic nucleobase modes on magnesium oxide and olivines have been used to determine nucleobase orientation on these substrate materials (Figure 14) [44, 52]. Other examples of mode disappearance occur commonly [e.g., 46, 47, 53]. Adsorbate and substrate modes can also coalesce upon adsorption [46]. On the other hand, adsorbates can modify the substrate's surface states, give rise to new electron states, and alter its surface chemical activity [e.g., see 37 and references therein].

Adsorbate/substrate systems exhibit a significant sensitivity to locality specific effects. Adsorbate mode frequencies depend sufficiently on their specific adsorption site that spectroscopy can be used to identify adsorbate bonding locations, even to the point of being able to distinguish between adsorbates bound to crystal edges, faces, or corners [37, 42, 43, 54–56]. Substrate surface defects, which are localized by their very nature, influence the magnitude of adsorbate feature shifts and broadening, at least for polar molecules. The defect's nature, size and proximity to adsorbates play key roles in how significantly such defects alter feature properties [47, 48]. Figure 15 shows the predictions of Zorgati et al. [48] for how a vibrational mode of CO adsorbed onto magnesium oxide (MgO) is affected by increasing concentrations of MgO surface dipolar defects. Higher defect concentrations produce larger redshifts, increased broadening, and decreased maximum absorption in the CO mode.

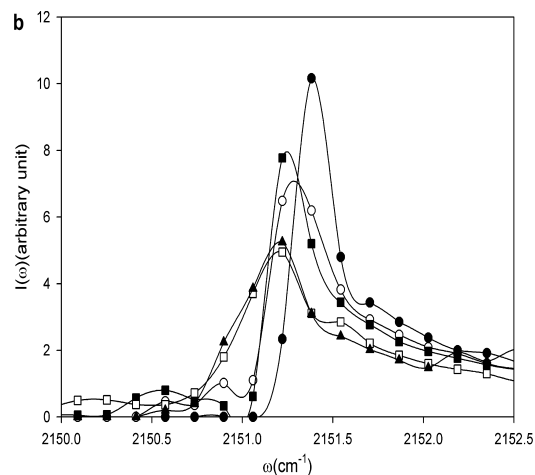


Figure 15: Predicted vibrational mode of CO adsorbed onto MgO in the presence of dipolar surface defects at defect concentrations equal to 0%, 1%, 3%, 10% and 15%, respectively. Reproduced from [48].

Adsorbate concentration is another important variable.

As adsorbate concentration increases, the mutual self-interactions between adsorbate molecules can become important. Numerous studies of CO adsorbed on various substrates have observed significant shifts in modes along with the transition of single-peaked to double-peaked features

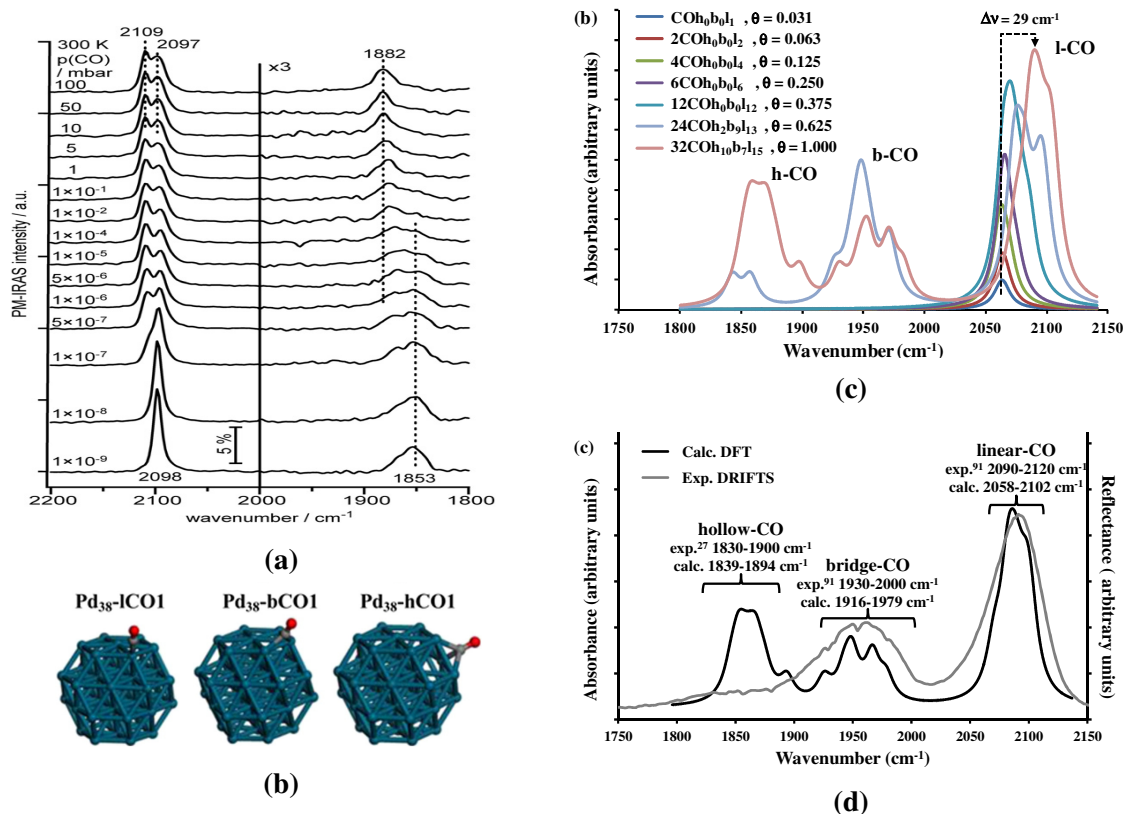


Figure 16: (a): The evolution of the reflection/absorption IR spectra of CO adsorbed onto platinum as a function of ambient P (a proxy for CO surface concentration); reproduced from Figure 3 of [42]. (b): Graphic showing the bonding of CO to Pd in the linear, bridge, and hollow (h-CO, b-CO, and l-CO, respectively) configurations. (c): Simulated IR absorbance spectra for CO adsorbed onto palladium as a function of total CO number and adsorption site. The peaks corresponding to each CO adsorption site are labeled. Note the peak shifts and morphology changes as CO coverage increases. (d): Comparison between experimental data and one of the calculations in (c). Figures (b)-(d) reproduced from [57].

with varying CO concentration [e.g., 42, 54]. These spectral variations are attributed to the changing strength of CO-CO interactions as CO concentration varies. Figure 16a shows a dramatic example of these effects in the case of CO adsorption onto platinum (Pt). The bands at 1853 cm^{-1} and 2098 cm^{-1} are characteristic of CO adsorbed at bridge and linear site locations (see Figure 16b). As CO surface concentrations increase, the 1853 cm^{-1} mode experiences a broadening and then splitting into two bridge modes that seems to be an indicator of a CO overlayer forming [42]. As the bridge mode transition is occurring, a second linear mode also appears, supporting the idea that new modes are being established in the forming CO overlayer. The *ab initio*

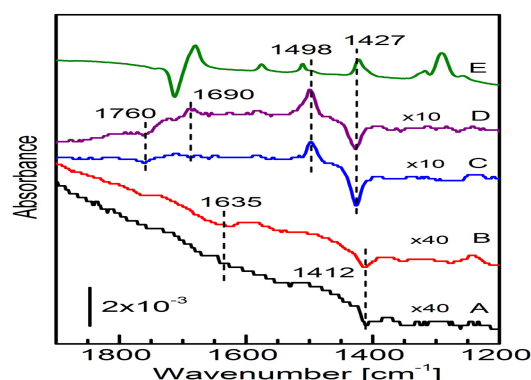


Figure 17: Spectra of TPA on rutile, going from submonolayer (A) coverage to a multilayer (E). Reproduced from [58].

modeling of Zeinalipour-Yazdi et al. [57] provides theoretical backing to this notion, predicting a concentration dependent variation in the propensity for CO to be adsorbed at different palladium (Pd) substrate sites, the evolution of multiple-peak features, and an overall concentration-dependent mode frequency shift (Figure 16c).

At sufficiently high adsorbate concentrations, the mutual interactions also give rise to new collective modes. Adsorbate monolayer formation will occur as the adsorbate concentration increases to effect full coverage of the substrate with further adsorption producing multi-layered coverage; the character of the collective modes evolves during this process as the influence of the substrate on the upper-surface adsorbate layers decreases [37, 58]. Figure 17 provides an example of this effect in the case of terephthalic acid (TPA) on rutile titanium dioxide (TiO_2). At low TPA coverage, two C-O stretching vibrations are present with new modes appearing as TPA dosage increases indicating the nascent formation of a monolayer. At even higher dosages, further modes appear and the spectrum begins to resemble that of isolated, solid TPA [58], indicating the influence of the TiO_2 substrate has substantially decreased on the regions of the TPA layers most strongly influencing the observed spectra.

3.1.2.2 Hydration

Because of the variable, yet nearly ubiquitous, presence of water in the terrestrial environment, we consider here examples of its interactions with other substances and the impact these interactions have on the \tilde{n} of the participating materials. The various themes concerning the impact of intermolecular interactions on \tilde{n} discussed in §3.1.2.1 appear again in this context; this is not surprising given that intermolecular interactions involving water are just a specific case of the prior, more general, considerations. In particular, \tilde{n} variations will be seen to depend on the details of the substrate media, the specific site to which H_2O molecules are bound, and the H_2O concentration. Above we explicitly only considered *surface* interactions between adsorbate molecules and substrates; relevant phenomenology in the present case also includes diffusion of H_2O into the bulk of the substrate. However, the impact on \tilde{n} of H_2O incorporation into the substrate's bulk shares qualitatively similar features to the impact of surface-only interactions.

A primary result of H_2O -substrate interactions is to produce frequency shifts in the location of H_2O absorption features and changes in the strength and shape of these features. The magnitude of these changes depends on the nature and strength of the bonds that H_2O molecules form both with the substrate and each other [60, 61]. For pure water, in the vapor phase, the H_2O fundamental symmetric stretching, bending, and asymmetric stretching modes—

ν_1 , ν_2 , ν_3 , respectively—occur at $\nu = 3657$, 3756, and 1595 cm^{-1} ($\lambda = 2.734$, 2.662, and $6.271 \mu\text{m}$; [62]). In liquid H_2O , the stretching bands are shifted to lower frequencies (ν_1 : 3280 cm^{-1} ,

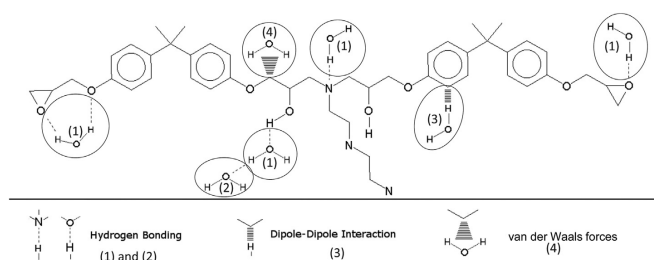


Figure 18: The various forms of bonding between H_2O molecules interacting with substrates. Reproduced from Figure 1 of [59].

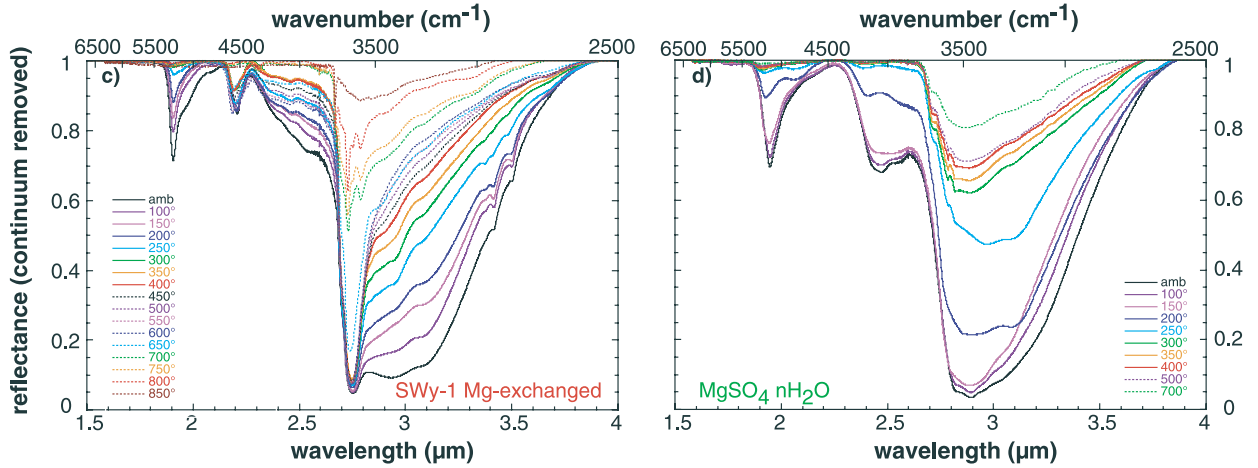


Figure 19: Reflectance spectra of hydrated montmorillonite clay (left-hand panel) and magnesium sulfate as the samples are heated, driving off sorbed water. Reproduced from Figure 7 of [69].

ν_3 : 3490 cm^{-1} ; [63]) and the bending mode to higher frequency (ν_2 : 1644 cm^{-1} ; [64]). The ν -shifts are due to hydrogen bonding [65] that tends to create short-lived tetrahedral molecular networks in the liquid phase [66]. Similar considerations apply in the solid phase, where the degree of crystallinity and T_{th} impact band location and strength[18, 67, 68].

The ν -shifts seen in H_2O -substrate systems similarly result from several different bonding mechanisms of varying strength, illustrated schematically in Figure 18 [59]. Direct hydrogen bonding between a H_2O molecule and a strongly polar region of the substrate molecule provides the strongest bond. Next is secondary hydrogen bonding where a second H_2O molecule binds to a polar region of the substrate via another, directly hydrogen-bonded H_2O molecule. Dipole-dipole interactions provide the next strongest bond, followed by the weaker bonding due to molecule-molecule van der Waals interactions. In addition to the fundamental stretching and bending bands, several H_2O overtone and combination bands near $\nu \approx 7000$, 5200 , and 4540 cm^{-1} ($\lambda \approx 1.43$, 1.93 , and $2.2\text{ }\mu\text{m}$) are particularly diagnostic of the relative importance of various bonding mechanisms in water-substrate systems across multiple substrate material classes.

For example, in smectite clays water can bind to clay interlayer surfaces, interlayer cations, and be adsorbed on to grain surfaces (in addition to the ubiquitous H_2O - H_2O bonding) [70]. Water interacting with such clays (see, e.g., the left-hand panel of Figure 19) show splitting of the fundamental bands that are interpreted as being due to cation bound versus adsorbed H_2O molecules [70–75]. The $\lambda \approx 1.43$ and $1.93\text{ }\mu\text{m}$ combination/overtone bands exhibit the same splitting [72, 74, 75]. Both H_2O -bonding types can be present simultaneously in the clay. The broad class of silicate (SiO) minerals can be hydrated to various degrees with H_2O bonding through direct or indirect hydrogen bonding and dipole-dipole interactions, each of which exhibits absorption bands at different frequencies [76–78]. The 1.9 and $2.2\text{ }\mu\text{m}$ combination bands again exhibit λ -splitting attributed to the two hydrogen bond types [79, 80]. Studies considering H_2O interactions with various polymers come to similar conclusions concerning the presence of two or more H_2O -polymer bonding mechanisms based on ν -shifts and evolution of various band components as a function of hydration level [59, 66, 81–90].

As the H_2O concentration in one of these systems is varied, the relative contribution to the overall absorbance made by differently bonded H_2O molecules changes. For Na- and Mg-montmorillonite

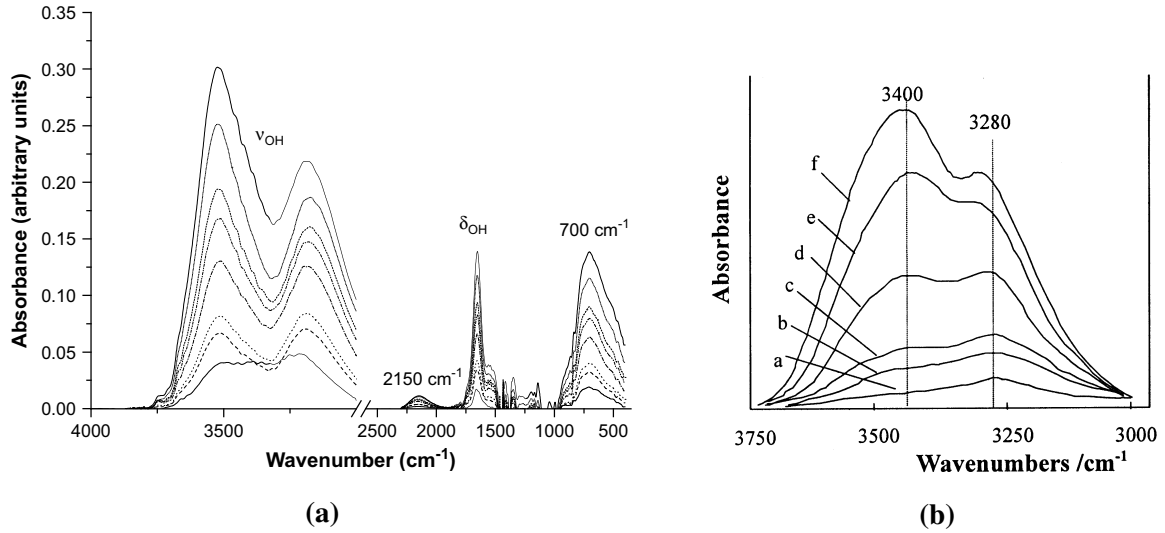


Figure 20: (a): Evolution of absorption bands in a PP/EVOH film as its hydration increases; reproduced from Figure 3 of [84]. (b): Changes in the hydroxyl stretching mode of PVA membrane for different degrees of hydrations; reproduced from Figure 6 of [82].

(smectite clays), the evolution of the two $1.9 \mu\text{m}$ bands under varying hydration levels demonstrates a structural change with a feature-shoulder due to the $\lambda \approx 1.96 \mu\text{m}$ band disappearing at low hydration levels, while the $1.91 \mu\text{m}$ feature remains, albeit at lower strength (left-hand panel of Figure 19). This is interpreted as implying the $1.96 \mu\text{m}$ band being due to surface adsorbed H_2O while the $1.91 \mu\text{m}$ being produced by the tightly bound interlayer surface and cation H_2O molecules that requires significant dehydration to drive off [69, 70]. A similar trend occurs for the splits in the ν_1 -band located at $\lambda \approx 2.83$ and $2.98 \mu\text{m}$ in the same Figure 19 panel, with the $2.83 \mu\text{m}$ band that creates the shoulder in the large $\lambda = 2.75 \mu\text{m}$ feature produced by the more tightly bound H_2O molecules. The $\lambda = 2.2 \mu\text{m}$ band in the same system is produced by Mg-OH direct hydrogen bonds and persists until very significant dehydration occurs. The right-hand panel of Figure 19 shows similarly the spectral variations of magnesium sulfate at various levels of hydration; the differences in H_2O band shape and evolution relative to the $\text{Mg-montmorillonite}$ highlight the fact the substrate material strongly influences the morphology of the OH features. In silicate minerals, lower water concentrations lead to SiOH features becoming more apparent relative to non-bonded water features [91].

In polymers, the ν_1 and ν_3 frequencies tend to shift to lower-frequencies with increasing bond strength between a H_2O molecule and the substrate [84]; so, e.g., for H_2O in polypropylene-poly(ethylene-co-vinyl alcohol) (PP/EVOH) mixtures, the stretching bands develop two peaks, one in the $3520\text{--}3530 \text{ cm}^{-1}$ range produced by unassociated and weakly bound H_2O and another near 3200 cm^{-1} associated with H_2O hydrogen bonded to polar groups within the polymer, as shown in Figure 20. Lines in this figure correspond to spectra obtained at different times during a water sorption process. The 3200 cm^{-1} peak predominates at first and is then overtaken by the 3500 cm^{-1} peak as time goes by, indicating that as water diffuses in the substrate, direct hydrogen bonds form first, followed by weaker indirect hydrogen bonding. The weaker bonds continue forming at a faster rate as water content increases [84; 85–87, 92 report similar findings]. This behavior appears similar to a saturation effect noticed by Ping et al. [82] in their study of water in hydrophilic polyvinyl alcohols (PVAs); there up until some critical water concentration,

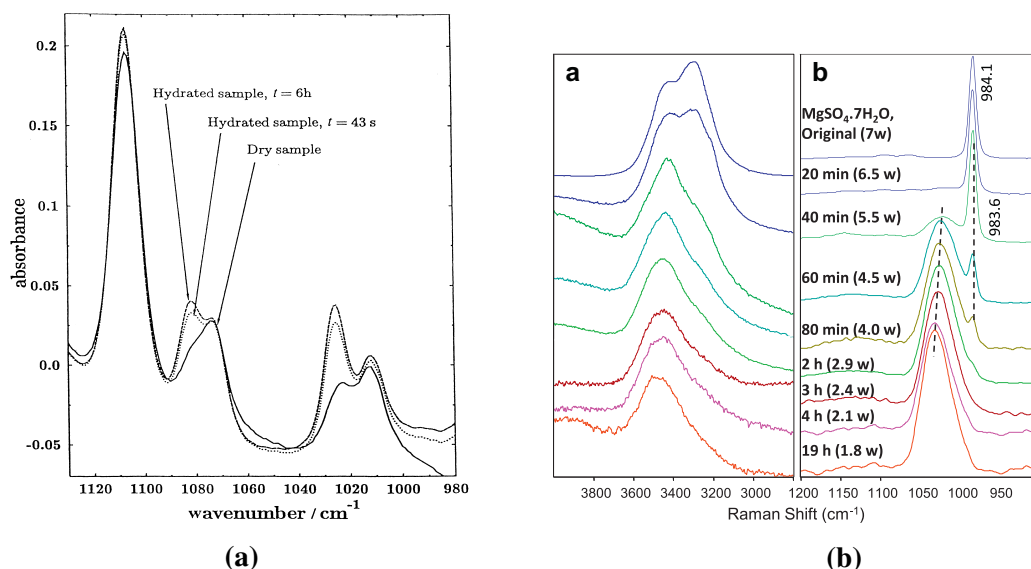


Figure 21: (a): Changes in polyether sulphone $\nu(\text{SO}_3^-)$ bands with increasing hydration; reproduced from Figure 8 of [66]. (b): Evolution of hydrated MgSO_4 spectra with changing degree of hydration; reproduced from Figure 6 of [97].

only strongly bound H_2O molecules were present. Above this concentration, the number of H_2O molecules directly bound to the polymer quickly saturates while weakly-bound H_2O molecules appear and continue to increase in number. The number of strongly-bound H_2O molecules at saturation depends on the polymer involved and reflects the overall ability of a polymer's polar groups to interact with H_2O in the polymer matrix. A different H_2O binding order was observed for water diffusing into a polyhydroxyalkanoate, where H_2O molecules first diffuse into the microvoids in bulk water form or are dispersed on the surface in free water form, and then penetrate into the polymer matrix and hydrogen bond with the polymer's hydrophilic groups [90].

Water diffusing into a substrate material can affect the substrate's structural and chemical properties. Exposure to water can lead to hydrolysis in some polymers and alter the polymer's intrinsic hydrogen-bonding interactions[82, 93, 94]. Water sorption causes polymer to swell [87], decreasing polymer crystallinity, increasing molecular mobility, and reducing glass transition temperatures [95, 96], particularly in hydrophilic polymers [82]. Such structural changes have corresponding impacts on spectral feature locations and morphology. E.g., Schoonover et al. [93] reports shifts in N-H and carbonyl group modes' frequencies as a function of hydration in a poly(ester urethane). Other frequency-shifts in various polymer groups are reported in [82, 90]. Figure 21a shows an example of hydration-induced shifts in the symmetric $\nu(\text{SO}_3^-)$ band in a polyether sulphone [66]. In hydrated sulfate minerals, changes in hydration can initiate changes in crystal structure [97], again leading to variations in spectral features. Figure 21b provides an example of variations in H_2O and SO_4 bands in epsomite as the sample's hydration is reduced. The disappearance of the 983 cm^{-1} peak and appearance of a peak near 1025 cm^{-1} (that shifts to higher ν as dehydration continues) is due to a phase change that occurs due to the loss of one H_2O molecule per epsomite that is not coordinated with a Mg cation [97].

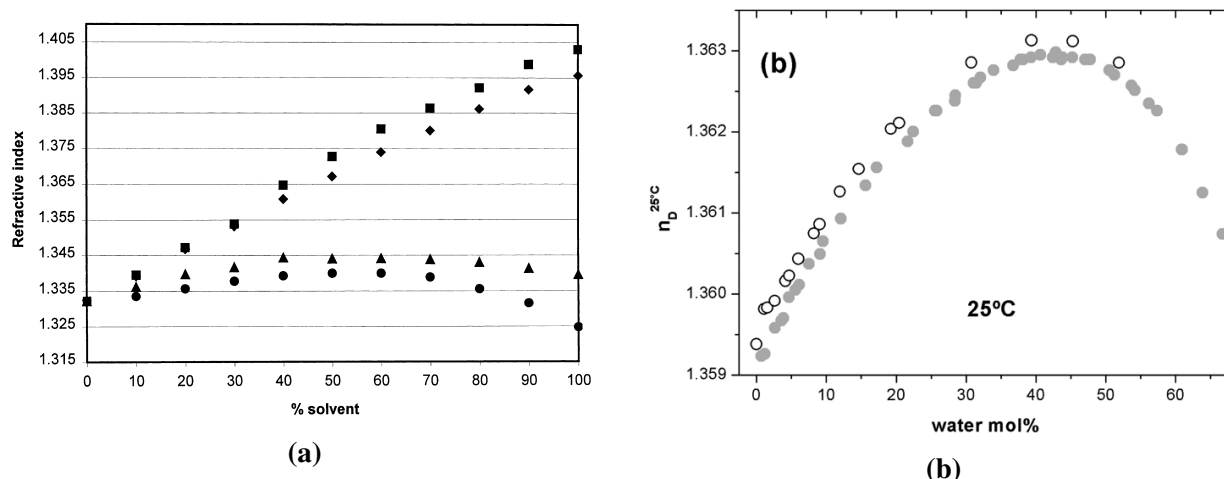


Figure 22: (a): Changes in solution n ($\lambda = 254$ nm) with solvent mixing fraction for 1,3 dioxolane (diamonds), acetonitrile (triangles), THF (squares), and dichloromethane (circles); reproduced from Figure 6 of [98]. (b): Changes in solution n with H_2O mol% for water-ethanol mixtures; reproduced from Figure 3 of [99].

3.1.2.3 Interactions in Liquid Solutions

A substance in solution experiences a significantly different distribution of intermolecular forces than when in isolation. As in the two cases examined so far, the change in potentials seen by both solute and solvent molecules in a solution can lead to changes in both component's \tilde{n} and the overall spectral characteristics of the solution.

As in the case of adsorption, where adsorbate concentration influences \tilde{n} behavior, solute concentration is also an important variable. For example, the n of liquid mixtures varies as a function of the mixing ratio of the solution. Examples of such behavior are shown in Figure 22 [98]. In the case of solutions of 1,3 dioxolane (diamonds) and THF (squares) in water, the variation of n with solvent mixing fraction is monotonic between the n of the individual components. However, aqueous solutions of acetonitrile and dichloromethane (triangles and circles) exhibit a non-monotonic n that peaks near a 50/50 mixing ratio and that exceeds the index of either pure liquid. Water-ethanol solutions exhibit similar behavior as seen in Figure 22b [99]. This non-monotonic behavior would appear to indicate that new energy states are being generated by solute-solvent interactions.

The absorption features of a compound in isolation versus in solution show shifts in ν due to interactions between the solvent and solute [e.g., 47, 102–106, for a small sample]. This behavior is so common that multiple constructs have been developed to quantitatively describe the observed shifts [e.g., see references in 102, 107]. Band shifts and band shape variations are dependent on the solvent materials [see Figure 23a; 100]. Solute-solvent interactions may also produce solute molecule conformation changes [108]. Additionally, there are examples of solute absorption features splitting in solution. Further, the ν -separation between such split-modes can depend on solute concentration Hernández et al. [106]. In Hernández et al. [106], the authors proposed the observed mode splitting mechanism to be solute-solute interactions that indirectly involves water molecule complexes interacting with several different groups in the solute molecules. Finally, the *solute's* band shapes and positions can also depend on solution concentration [see Figure 23b; 100, 101].

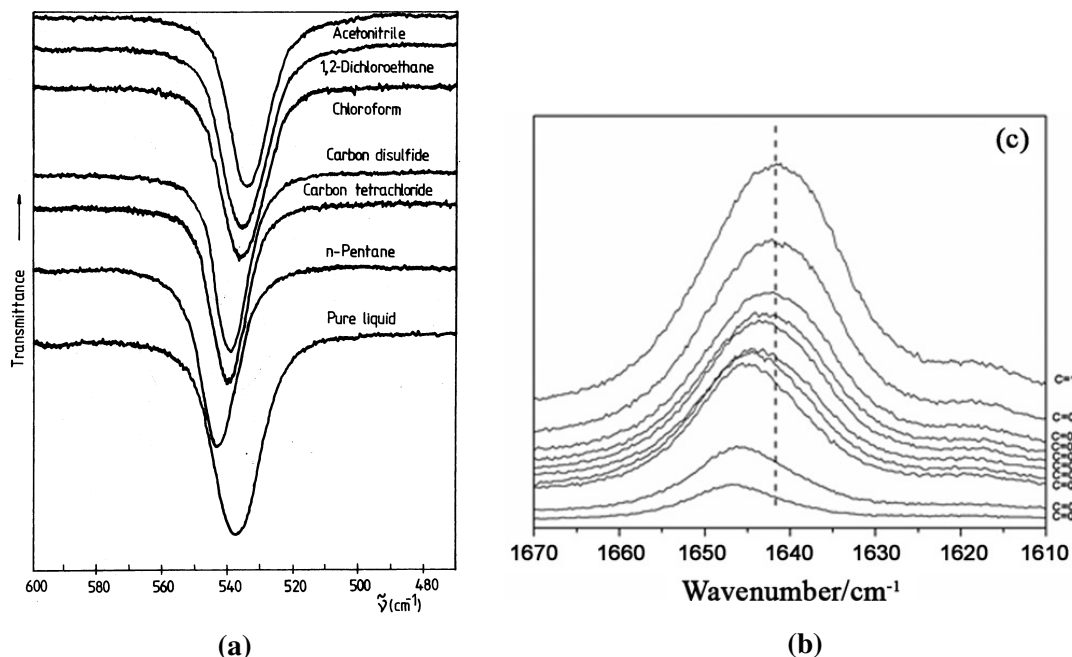


Figure 23: (a): The transmission spectra about the $\nu(\text{C-Br})$ band of 2-bromopropane in the indicated solvents showing how the band's shape and location depend on the solvent; reproduced from Figure 1 of [100]. (b): The carbonyl stretching mode of 2'-hydroxyacetophenone in carbon tetrachloride at different solute concentrations; reproduced from Figure 5 of [101].

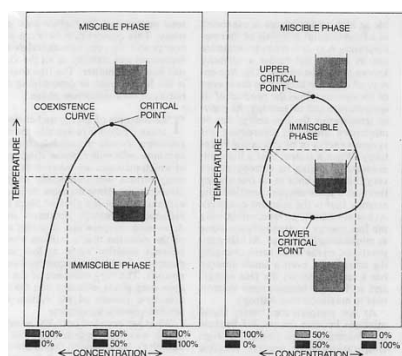


Figure 24: Prototypical phase diagrams for binary liquid mixtures. Reproduced from [109]

The miscibility of binary liquid mixtures is another phenomenon that could have interesting implications for a solution's spectrum. In general, the miscibility of binary liquid mixtures exhibits a dependence on temperature that can be described by a phase diagram similar to left-hand side of Figure 24 [109]. At sufficiently high temperatures, the mixture is totally miscible. As the temperature is lowered, a phase transition occurs and the single solution separates into two phases of different concentration ratios, and therefore different refractive indices. At the interface of the two phases, reflection will occur due to the mismatch in refractive indices in the two phases. As the phase diagram shows, the concentration ratios of the two phases, and therefore the corresponding \tilde{n} , exhibits a T_{th} -dependence throughout the phase diagram, translating to a temperature dependent reflectance at the interface between the two phases. In some special cases, the coexistence curve will form a closed loop as shown on the right in Figure 24, where the liquids will return to a single miscible phase below some lower critical T_{th} .

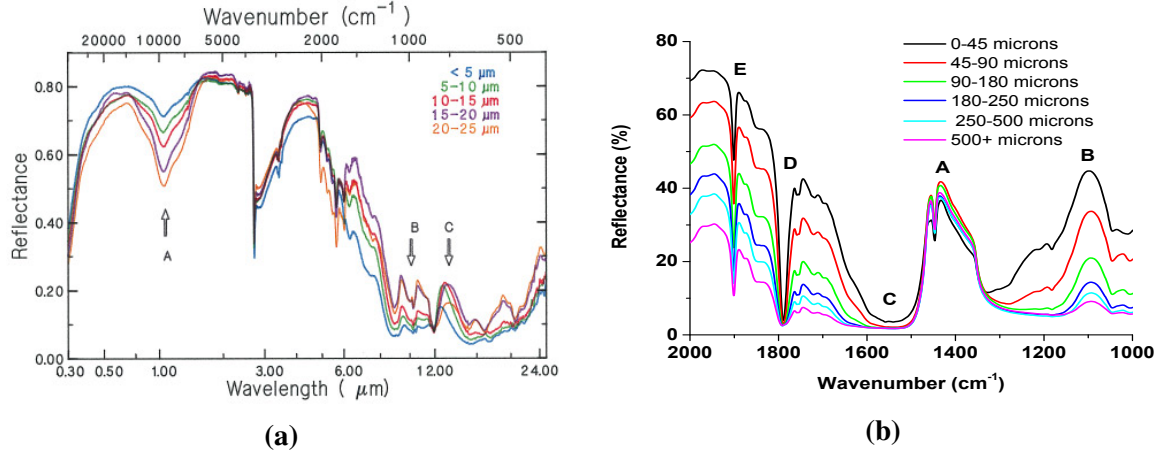


Figure 25: (a) Reflectance of an olivine sample as a function of particle diameters $a < 25 \mu\text{m}$; reproduced from Figure 4 of [120]. (b): Reflectance of a sodium nitrate sample as a function of particle size; reproduced from Figure 2 of [112].

3.2 Extrinsic Factors

3.2.1 Particle Size Effects

In the case of solid particulate media, there is a large body of literature on the variation of spectral signatures with particle size [9, 110–128] and how the spectra of particulate versus bulk samples of the same substance differ [129–132]. The underlying physics that qualitatively determine these variations was essentially captured by the discussion on stacks of multiple planar slabs connected to Figure 6 in §2. Given the three-dimensional geometry, irregularities in particle shape, and particles being packed densely enough to be within each other’s near-field scattering zone [which alters the effective scattering properties of each particle; e.g., 133], the quantitative details are much more complex here relative to §2. However, qualitatively the strength of scattering at each particle interface relative to the amount of absorption experienced within each particle’s volume still remain the primary factors that generate the observed spectral signature trends with particle size [e.g., see 134, 135, with the caveats that their description of scattering in terms of “specular” and “volume” components does not cleanly map to the underlying physical principles of the problem and that their developed theoretical model is not a quantitatively correct first-principles treatment for scattering in particulate media].

Figure 25 provides two examples of typical reflectance spectra variations with particle size. Again, these mirror very closely the trends observed in Figure 6. Figure 25a shows the reflectance of a silicate (olivine) for extremely fine size-separate ranges ($< 25 \mu\text{m}$ particle diameters). For $\lambda \lesssim 3 \mu\text{m}$, the samples’ overall reflectance increases and the strength of the large absorption feature at $\lambda \approx 1 \mu\text{m}$ decreases with decreasing particle diameter, a . The overall reflectance increase is consistent with the increased scattering expected as more particle boundaries per unit sample thickness are encountered with decreasing a . The decreasing spectral contrast is indicative that the combination of a and κ are such that the particles are optically thin across the entire band. For larger particles, this may not be the case and the possibility for feature-strength evolution with a that is not monotonic could arise. The evolution of the $\lambda \approx 1 \mu\text{m}$ feature in the pyroxene silicates enstatite and diopside reported in Mancarella et al. [113] shows an increase in feature strength with

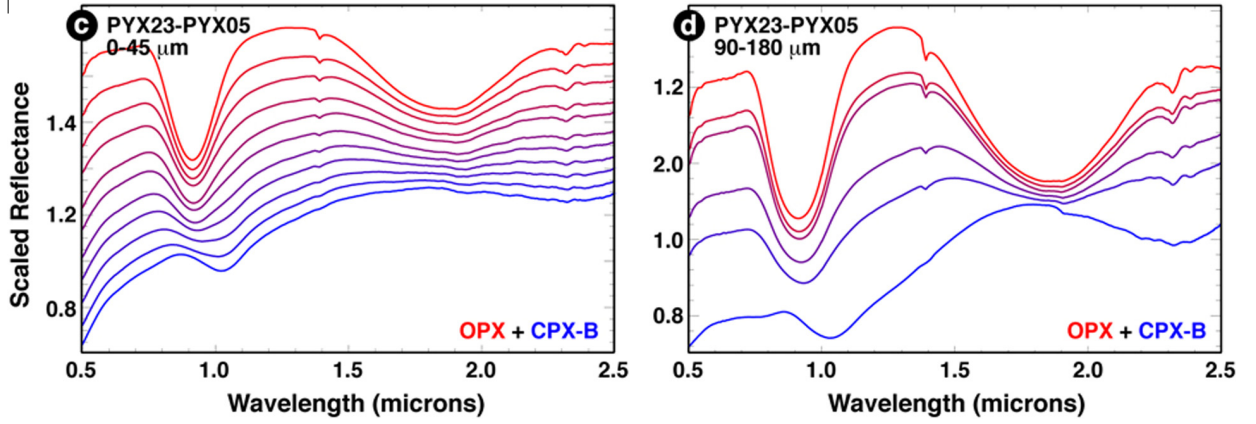


Figure 26: Reflectance spectra of two-component intimate mixtures of the orthopyroxene enstatite (OPX) and clinopyroxene diopside (CPX-B) with different lines showing relative weight increments of 10 and 20% for the 0-45 μm and 90-180 μm sized particles, respectively. The reflectances are scaled and shifted for clarity. Reproduced from Figure 5 of [111].

decreasing a over the range $a \approx 50\text{--}500\ \mu\text{m}$ for both minerals. This would indicate that for olivine, if larger particles had been included in the sample, a non-monotonic evolution in the $1\ \mu\text{m}$ band would likely be observed. For $\lambda \gtrsim 3\ \mu\text{m}$, a reversal in the overall reflectance versus particle-size behavior begins to appear: as λ increases, the highest reflectance corresponds to larger a . This behavior, which was not explored quantitatively in §2, is consistent with expected behavior for $\lambda \gtrsim a$. In this regime, closely packed particles with a and separations smaller than λ present an increasingly homogeneous medium to the EM-waves, decreasing scattering efficiency.

Figure 25b shows the reflectance of a series of sodium nitrate samples with a ranging from $< 45\ \mu\text{m}$ to $> 500\ \mu\text{m}$ [112]. Again, the overall reflectance of these samples increases for smaller a , except in the region between $\nu \approx 1300\text{--}1500\ \text{cm}^{-1}$. Over this particle size range, the various bands exhibited show several different behaviors. The $1901\ \text{cm}^{-1}$ feature shows evidence of non-monotonic spectral contrast variations with changing a . On the other hand, the $1798\ \text{cm}^{-1}$ feature, which is expected to be a stronger absorption band [136], shows increasing spectral contrast with smaller a for the entire particle-size range, indicating the center of the band remains optically thick even at the smallest a used. The peak reflectance in the $\nu \approx 1300\text{--}1500\ \text{cm}^{-1}$ is a so-called reststrahlen feature produced by the large κ -value of the molecule's primary vibration band. In other words, the absorption in this region is so-large that even the smallest particles essentially act as semi-infinite media and only the first-surface interface contributes to the scattering. At these wavelength ranges, the condition that $n \gg \kappa$ assumed in §2 does not necessarily hold. As such the detailed shape of the reflectance peak in this ν -region could depend on both the n and κ values there. See Myers et al. [112] for a discussion of the features near 1097 and $1540\ \text{cm}^{-1}$.

3.2.2 Optically Thin Samples in Mixtures

Samples containing optically thin components in proximity to other materials (e.g., small particles of two or more substances in a physical mixture, small particles on substrates, thin films on substrates) can have their spectral signatures modified by the presence of the proximate media. Put another way, the spectral signature of an optically thin sample in many contexts can change

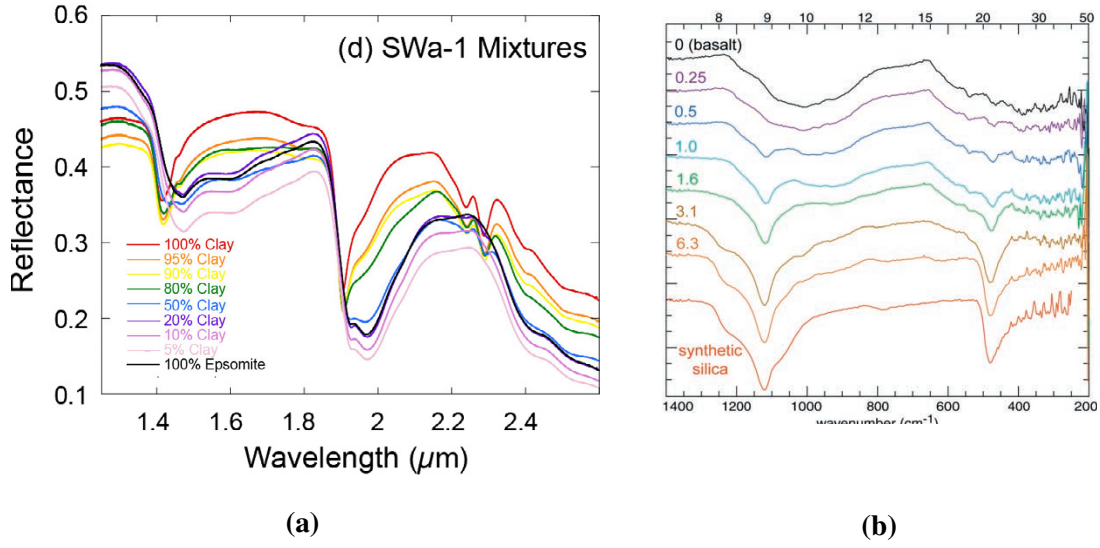


Figure 27: (a): Intimate mixtures of epsomite and a montmorillonite clay with composition expressed in clay mass fractions; reproduced from Figure 2 of [138]. (b): Emissivity of amorphous silicate thin layers (thickness specified in the plot in μm) on basalt; reproduced from Figure 2 of [139].

depending on its surroundings. We saw an example of this for the one-dimensional planar slab in Figure 5 where a change in substrate material altered the slab's R_{12} single-interface reflectance. Similar effects are present when media interfaces are in each other's near-field scattering zone, leading to changes in individual media scattering properties [133, 137].

The typical reflectance signature phenomenology in these optically-thin mixtures is for the combined reflectance spectra to evolve between the mixture's individual components' spectra as a function of mixing fraction. However, this evolution oftentimes exhibits a significantly non-linear dependence on component mixing fraction [140–143]. This should not be surprising given that the planar sample case exhibits an exponential dependence on slab thickness when $\kappa \neq 0$. Figure 26 provides an example—for the case of a mixture of the pyroxene minerals enstatite and diopside—of the non-linear evolution and spectra morphology changes that can occur in so-called intimate mixtures of small particles. The depth of the $\lambda \approx 1.0 \mu\text{m}$ enstatite (marked as OPX for orthopyroxene) feature in these figures is non-linear in enstatite mass fraction [111]. Additionally, the combination of the enstatite and diopside $1.0 \mu\text{m}$ features, which are shifted relative to each other, results in an evolution of the band position and morphology in the mixtures. The reflectances in this figure are scaled and shifted, which obviously hides the details of the relative reflectance evolution.

Figure 27a [139] provides one example of a sequence of intimate mixture spectra on an absolute reflectance scale. The mixtures in this case are of a montmorillonite clay and epsomite (a hydrated sulfate). Of particular note in this example is the fact that the reflectances of the intermediate mixtures are *not bounded* by the pure-material reflectances. This is by no means a special case—at least several of the mixtures examined in [111] exhibit similar behavior in absolute reflectances. We are not, however, in a position to comment authoritatively on the underlying physical causes of this behavior. The models typically used to interpret particulate mixture spectra [7, 144] are phenomenological in nature and do not predict such unbounded mixture spectra, while appropriate

first-principles EM-scattering methods [e.g. 133, 145] have not been applied to this problem in sufficient detail to provide a clear physical picture of how unbounded mixture spectra can arise.

Figure 27b provides an example of a thin film of amorphous silicate on a basalt substrate showing emissivity as a function of silicate layer thickness [138]. These authors again find the mixture spectra to depend on the component abundances (in this case, measured by layer thickness) in a non-linear manner. It is worth noting that thin film coatings are a spontaneously generated context in which coherent interference effects may likely impact spectral signatures. Awareness of this possibility is necessary for proper interpretation of spectra in cases where coherence effects could appear [146].

3.2.3 Other Sample Morphology Effects

Besides particle size in the case of a particulate medium, a sample's morphological properties can, more generally, influence its spectral signature. A readily available example is sintered polytetrafluoroethylene (PTFE) that is used as a reflectance standard that provides an $R \approx 0.99$ across the visible and near-infrared (VNIR). PTFE however is a non-absorptive material with an $n = 1.35$ across this range of the spectrum; i.e., a homogeneous thin slab PTFE would be essentially transparent. The key here is that sintered PTFE is not a homogeneous material, but has significant porous microstructure on $\sim 1\text{-}10\ \mu\text{m}$ spatial scale [e.g., 147]. This produces significant scattering for most λ in the VNIR that combined with a sufficiently thick PTFE sample results in a nearly spectrally flat, $R \approx 1$ reflectance. Moroz et al. [121] provides another example of internal structural impacts. They synthesized palagocite glasses through several pathways, one of which introduced significant porosity into the resulting samples. The high-porosity samples tended to have higher reflectances and show lower spectral contrast than the other glasses.

The impact of particle-shape on individual particle scattering properties has a large body of associated theoretical literature [e.g., 148–163]. However most of this work is focused on the impact of particle shape on the geometry of the scattered fields off a single-particle. Making the connection between these properties and how they impact a sample's spectral characteristics, even in the case of a single particle, remains an unfinished task. A few notable exceptions here include Kleiber et al. [164] who provide one example of how particle shape variations impact spectra, showing that relatively significant shifts in extinction peak locations can occur with variations in aspect ratios of spheroidal particles. Kiomarsipour et al. [165] describe the effect particle shapes have on the reflectance properties of zinc oxide powder based pigments. In particular, the particle-shape influences overall reflectance levels, some aspects of the spectra's general shape, and the strength of spectral features. In addition, Mishchenko [166] provides an example of theoretical effort to connect individual particle-shape effects (amongst other relevant particle properties) to the overall radiative transfer properties of a bulk particulate layer.

For bulk surface interfaces, surface roughness can influence spectral signatures. Kirkland et al. [167] compared the emissivity of limestone samples with smooth versus roughened surfaces. The roughened surface reduces the emissivity contrast in the limestone absorption bands and introduces an additional kink in the two bands present. Osterloo et al. [168] conducted a similar study but on a sample of 12 different natural rock surfaces and considering a range of surface roughness. Again, a trend of decreasing spectral contrast with increasing surface roughness was observed. Other studies have noticed the same trends in the case of carbonates [169] and chert [170].

3.2.4 Illumination and Viewing Angles: Sample BRDF

As demonstrated in §2, the quantitative details of a sample's spectrum vary with changing illumination and viewing angle. In the idealized case presented there, the reflection is exclusively specular—that is, the reflected light is directed at an angle from the surface normal equal to the angle of incidence. At angles other than this specular angle, no reflected signal would be observed. In less idealized situations, both surface and interior sample inhomogeneities lead to so-called diffuse scattering in non-specular directions. The distribution of scattered light intensity as a function of incident and viewing angles is described by a medium's bidirectional reflectance distribution function (BRDF). For real surfaces, the BRDF can be very complex (e.g., Figure 28).

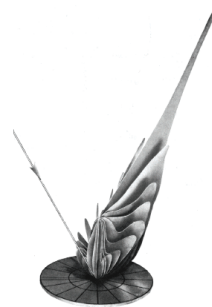


Figure 28: The BRDF of a roughened aluminum surface. Reproduced from [171].

Because of this complexity, direct measurement is the preferred method of capturing a medium's BRDF. However, this isn't always feasible, and more general situations need to be explored and various first-principles, descriptive, or empirical BRDF models are often employed [172]. Fundamentally, the BRDF captures light-matter interactions which strongly depend on the size of in-medium inhomogeneities relative to λ . As such, BRDF models are typically valid only over specific λ -ranges. Of such models, there are several that are particularly relevant in the IR spectral region, both descriptive [173–175] and theoretical [176–181]. Of media morphological properties, surface roughness plays an important role in setting the BRDF [e.g., 182, 183] and is a primary parameter in several of the theoretical models [e.g., 174, 178, 179]. In the near-IR, several additional BRDF models developed for particulate media are widely employed [7, 184]. Additionally, the Beard-Maxwell [178] and Ashikhmin [174] models are understood to provide reasonable representations of a painted surface BRDF (e.g., painted automobile surfaces).

Both the specular and diffuse reflectance components should vary with λ given the considerations in §2 and those given here. However, there is not a large body of literature explicitly documenting variations in BRDF with λ , which would be exhibited most directly by a medium's spectral shape and/or contrast being illumination and/or viewing geometry dependent. Suter et al. [185] provide examples of such angle-variant spectra in the case of explosive residues coating a surface. BRDF λ -dependence has also been documented to a lesser-or-greater degree in the case of VNIR measurements of grass-covered surfaces [186], asphalts and concretes [187], various sands [188], and snow [189]. In the IR, several studies have reported λ -dependent BRDF effects in the emissivity of quartz, both in particulate and polished slab geometries [129, 190]. In both cases, the quartz absorption feature depth increased with increasing look angle (that is opposite the trend in decreasing feature depth seen in reflectance of planar slabs in §2).

4 Spectral Signatures of Example Explosive and Chemical Warfare Agent Related Compounds

In this section, we highlight information in the literature concerning the spectral signatures of compounds that are either used as, or are related to, explosive materials and chemical warfare agents. The detection and identification of such compounds at trace abundance is of obvious interest from a public safety/security perspective.

Ethylene Glycol Dinitrate

Ethylene glycol dinitrate (EGDN) has similar properties to nitroglycerin and has been used in the manufacturing and testing of explosives including dynamite and plastic explosives such as Semtex. Recent work by Macleod et al. [191] measured the transmission spectra of EGDN in vapor phase. Their mid-IR measurement is shown in Figure 29 and compared to the condensed phase (in this case, liquid-phase) measurement taken from a database of explosive materials maintained by the University of Rhode Island (<http://expdb.chm.uri.edu>). It is readily apparent from Figure 29 that there are significant differences between spectral band positions and shapes between the condense and vapor phase forms of EGDN.

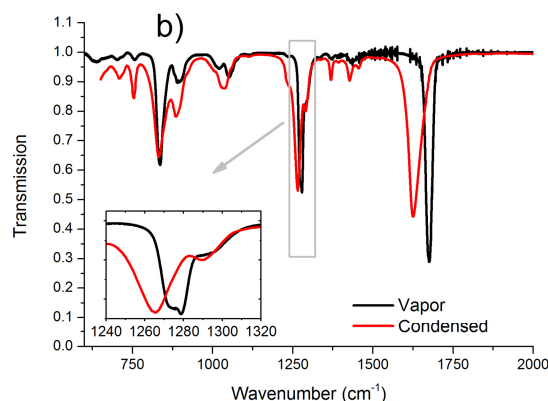


Figure 29: Transmission spectra of EGDN in vapor and condensed phase. Reproduced from [191].

Pentaerythritol Tetranitrate

Pentaerythritol tetranitrate (PETN) is a powerful explosive material and is similar in structure to nitroglycerin. In [192] the variability in the spectral signature and detection limits of PETN was studied as a function of angular dependence between source-target and target-detector, substrate type, and loading surface concentration. The spectra were recorded at a stand-off distance of 1 m over the range $\nu = 700\text{--}4000\text{ cm}^{-1}$. Two substrates were considered: anodized and polished aluminum. The differences between the two substrates influenced the reflectance spectra in multiple ways. Figures 30a and 30b show the PETN reflectance at a normal view-angle vs. surface concentration on the polished and anodized substrates, respectively. Stark differences can be observed between the reflectance spectra of PETN on the two substrates. For example, in the case of the $200\text{ }\mu\text{g cm}^{-2}$ samples (Figure 30a solid, Figure 30b outlined) the spectral peaks are almost completely inverted between the two substrates (additionally providing a particularly dramatic example of the importance of the surrounding environment in the case of optically thin target samples). Additionally, the reflectance spectra vary wildly as a function of PETN concentration in the case of the anodized substrate, whereas on the polished surface there is simply a shift in magnitude in the reflectivity as a function of concentration. The authors also explored the limit of detection as a function of source-to-target and target-to-detector angles. Again, the trends between the polished

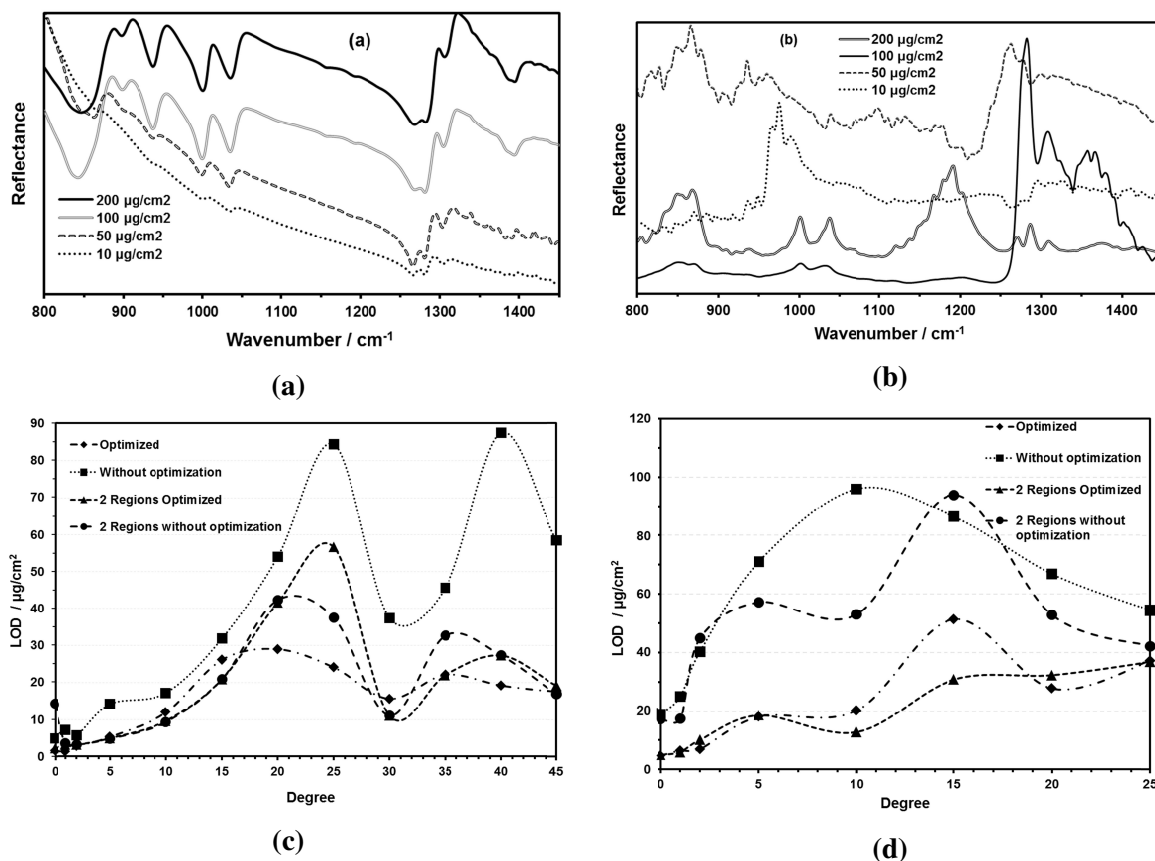


Figure 30: Mid-IR reflectance spectra of PETN on polished (a) and anodized (b) aluminum substrates. Limit of detection (LOD) as a function of incident angle for polished (c) and anodized (d) aluminum substrates. Reproduced from [192].

(Figure 30c) and anodized (Figure 30d) substrates show a marked difference (which the authors were not able to completely understand or explain).

Cyclotrimethylene Trinitramine

Cyclotrimethylene trinitramine (RDX) serves as a base for a number of military explosives including Semtex and mixtures of RDX and TNT (e.g., Cyclotol, HBX, H-6, etc.). Figure 31 shows a reference absorbance spectrum of RDX; note that as pointed out in [194], the features between $\nu \approx 1250\text{--}1700\text{ cm}^{-1}$ lie in strong H_2O vapor absorption bands and will not be readily seen in stand-off detection scenarios. Liu et al. [195] explored the reflectance spectra of surface adsorbed RDX on stainless steel. Figures 32a and 32b show optical images and reflectance spectra, respectively, of freshly deposited RDX.

While Figure 32 shows that there is variability in the intensity of the reflectance spectra measured from different spots (due to inhomogeneity of the deposition), the spectral peaks are all aligned.

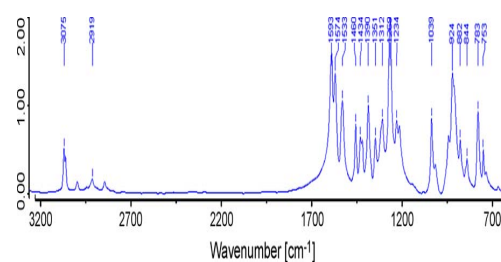


Figure 31: Absorbance of RDX. Reproduced from [193].

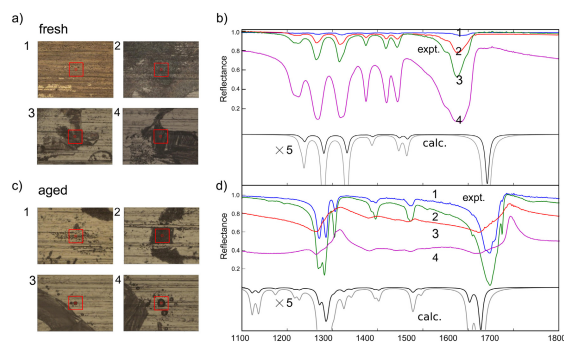


Figure 32: FTIR measurements of RDX - (a) Optical microscopy images of fresh RDX patches by droplet evaporation, Red squares are 50 x 50 microns, (b) FTIR reflectance spectra of fresh patches, (c) Optical microscopy images of 1-day aged RDX patches, (d) FTIR reflectance spectra of 1-day aged patches. Reproduced from [195].

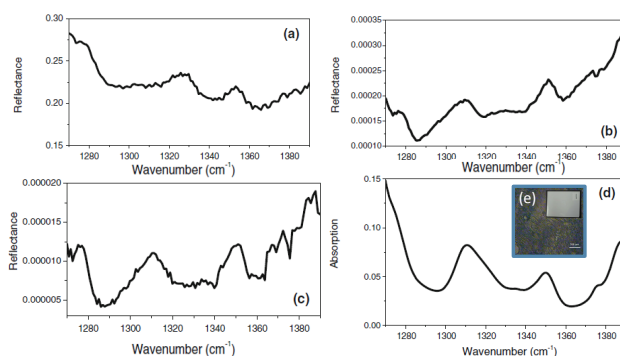


Figure 33: Reflectance spectra of RDX at 0 (a), 5 (b), and 40 (c) along with the absorption spectrum (d) over the same spectral band, (e) an optical microscope image of the RDX region demonstrating the surface texture of the sample on a car door. Reproduced from [185].

This however changes drastically for the RDX spectra that are a day old (Fig. 32c and 32d) with two of the spots exhibiting none of the spectral features visible in the fresh samples, which the authors attribute to a molecular conformational change in the crystal structure based on existing *ab initio* calculations of RDX equilibrium molecular geometry energetics.

Suter et al. [185] explored the angular dependence of the spectral signature of RDX at standoff distance of 2 meters using an external cavity quantum cascade laser. For these experiments the samples were sprayed onto a car door with a standard automotive finish of a white paint with clear coat. The reflectance data for RDX at a concentration of $81 \mu\text{g cm}^{-2}$ is shown in Fig. 33 for angles of 0, 5, and 40 degrees. The specular reflection spectrum (Fig. 33a) differs significantly from the two diffuse reflectance spectra, with the diffuse reflectance spectra resembling most closely the laboratory *absorbance* spectra. The specular reflectance, on the other hand, bears little resemblance to the laboratory measurements.

Thiodiglycol

Thiodiglycol (TDG) is a solvent used in a variety of industrial applications, but can also be used in the manufacture of chemical weapons (mustard gas). Because it can be obtained in small quantities, it is commonly used as a chemical warfare agent simulant. Reid et al. [196] measured the mid-infrared reflectance spectra of TDG using a broadband femtosecond optical parametric oscillator as the illumination source. They measured reflectance spectra for TDG deposited on concrete (Figure 34a) and black anodized aluminum (Figure 34b). Figure 34 clearly demonstrates not only a shift in the peak of the spectral band position, but also a change in shape of the spectral features between the two measurements. The dual peak is present in the reference spectrum and TDG on concrete but is clearly absent for TDG on the black anodized aluminum surface. It is important to note that the authors attribute the differences in the reference and measured spectra to a normalization error (not, e.g., to substrate \tilde{n} differences).

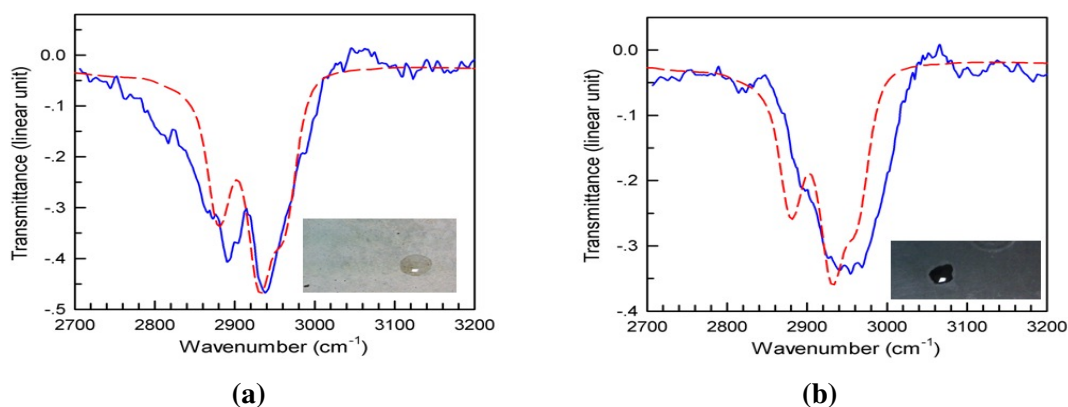


Figure 34: Reflectance spectra of TDG measured on concrete (a) and black anodized aluminum (b) at a standoff distance of 2 m (blue solid line) and a reference spectrum (red dashed line). Reproduced from [196].

Tetryl

2,4,6-trinitrophenylmethylnitramine (tetryl) is an explosive compound used primarily now for detonators and boosters. The absorption spectra of tetryl across the IR is shown in Figure 35 [194]. As with RDX, the most prominent spectral features occur in the $\lambda \approx 6\text{--}8\mu\text{m}$ ($\nu \approx 1250\text{--}1670\text{ cm}^{-1}$) range where H_2O absorption is strong. As such, stand-off detection of tetryl may also be challenging due to significant atmospheric absorption [194]. Suter et al. [185] explored the angular dependence of tetryl's reflectance spectral signature. Similar to their results for RDX, the specular reflectance component (Figure 36a) does not contain strong spectral features whereas the diffuse reflectance component over a large angular range (shown in Figure 36b and 36c) mimics the main absorption bands seen in the laboratory reference spectrum (Figure 36d).

Trinitrotoluene

Trinitrotoluene (TNT) is a commonly used explosive material. TNT reflectance spectra were measured by Suter et al. [185] using the same methodology as discussed above for RDX (Figure 33) and tetryl (Figure 36). While TNT's specular reflectance component (Figure 37a) doesn't exhibit the expected spectral features (similar to the RDX and tetryl results), the TNT diffuse spectral component has a different dependence due to sample morphology effects. Figure 37e shows that the TNT surface coverage is very homogeneous and smooth as compared to the RDX and tetryl residue morphologies (Figures 33e and 36e), resulting in a much smaller diffuse reflectance component which limits the SNR at larger angles.

Fuchs et al. [197] considered the reflectance spectra of TNT deposited on different substrates. Their results further demonstrate the impact of substrate properties on optically-thin target sample signatures, as already seen in the cases of TDG and PETN discussed above. In the Fuchs et al. [197] results, the substrate's influence on the TNT reflectance signature is particularly dramatic as seen in Figure 38, which shows the reflectance spectra of TNT on aluminum and car paint. There is a clear inversion in the spectra between the two cases due to the relative absorbance of the two substrates compared to the TNT sample.

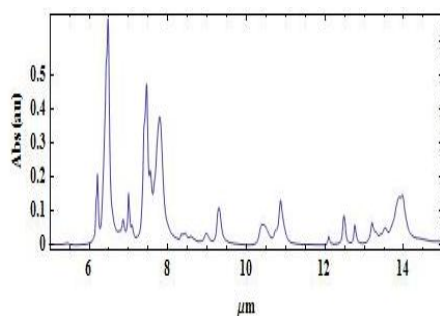


Figure 35: IR absorption spectra of Tetryl. Reproduced from [194].

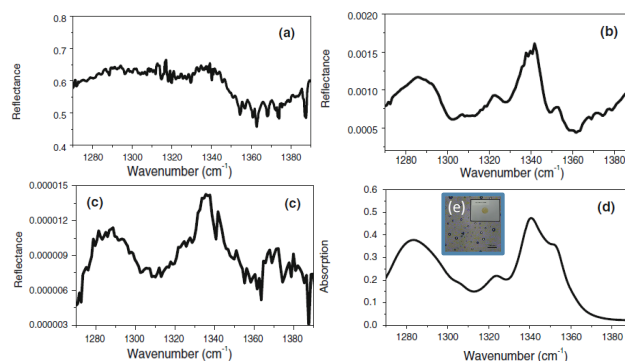


Figure 36: Reflectance spectra of a tetryl sample applied to a car door at 0° (a), 5° (b), 40° (c) and reference absorption spectrum (d); (e) an optical microscope image of the tetryl sample on a car door. Reproduced from [185].

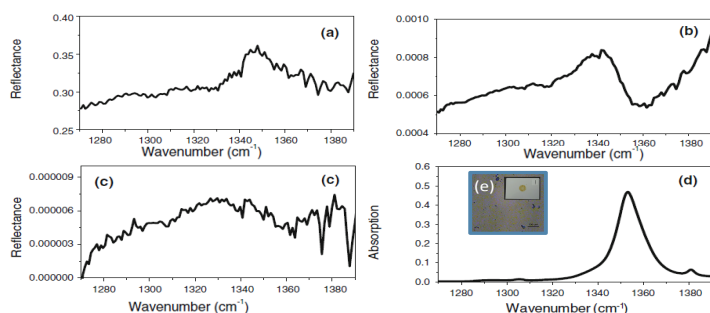


Figure 37: Reflectance spectra of a TNT sample on a car door at 0° (a), 5° (b), 30° (c) and reference absorption spectrum (d); (e) an optical microscope image of the TNT sample on a car door. Reproduced from [185].

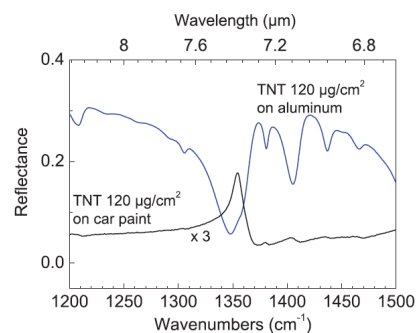


Figure 38: Reflectance of TNT at a concentration of $120 \mu\text{g cm}^{-2}$ on aluminum (blue line) and car metal paint (black line). Reproduced from [197].

This page intentionally left blank.

Appendix A Planar Slab Reflectance: Definitions, Notation, and Derivation

Here we provide the basic notation and develop the expressions required for the analysis of the incoherent spectral reflectance of a planar layer of finite thickness on an semi-infinite substrate, the essential geometry of which is shown in Figure 1 in §2. Consider a plane electromagnetic wave with electric field vector $\mathbf{E}(t, \mathbf{x}) = \mathcal{E} \exp(i\omega t - i\mathbf{k}_0 \cdot \mathbf{x})$ incident on the the sample (medium 1) at an angle θ_0 relative to the surface normal. Here \mathcal{E} , ω , and \mathbf{k}_0 are the radiation's vector amplitude, frequency, and wave vector, respectively, and t , \mathbf{x} indicate time and spatial position; the wave vector $\mathbf{k}_0 = (\omega/c)\hat{\mathbf{s}} = k_0\hat{\mathbf{s}}$ where $\hat{\mathbf{s}}$ is the unit vector along the wave's propagation direction and c is the speed of light. The wavelength in medium 0 is then given by $\lambda_0 = 2\pi/k_0 = 2\pi c/\omega$.

This wave's Poynting vector (i.e., energy flux with dimensions [energy area⁻¹ time⁻¹]) is $\mathbf{S}_0 = n_0 \epsilon_0^{1/2} |\mathcal{E}|^2 / (2\mu_0^{1/2}) \hat{\mathbf{s}}$, where $|\mathcal{E}|^2 = \mathcal{E} \mathcal{E}^*$ and \mathcal{E}^* denotes the complex conjugate of \mathcal{E} . For the calculation of reflectance, we will be interested in the components of \mathbf{S} normal to the sample interface. We denote these interface-normal components of the incident, reflected, and transmitted flux vectors as I_0 , I_R , and I_T . These interface-normal components depend on the wave's interface-parallel field components. For a wave incidence angle, $\theta_0 \neq 0$, these in turn depend on whether \mathbf{E} is in or perpendicular to the plane of incidence (also designated as p-polarized and s-polarized waves, respectively).

The expressions for reflectance, $R \equiv I_R/I_0$, and transmittance, $T \equiv I_T/I_0$, resulting for the two polarization state cases can be written in a unified manner in terms of the so-called tilted optical admittances η_j of the involved media [e.g., 11]:

$$\eta_j = \begin{cases} \frac{\tilde{n}_j}{\cos \theta_j} & \text{for p-polarization,} \\ \tilde{n}_j \cos \theta_j & \text{for s-polarization.} \end{cases} \quad (3)$$

The θ -quantities in two media j and k are related by Snell's law:

$$\tilde{n}_j \sin \theta_j = \tilde{n}_k \sin \theta_k, \quad (4)$$

and are, generally speaking, complex quantities. With the assumption that $\kappa_0 = 0$, the $\cos \theta_j \equiv a_j - ib_j$ for $j=(1, 2)$ may be calculated in terms of θ_0 explicitly as [following the notation in 198]:

$$a_j - ib_j = \sqrt{\frac{\sqrt{p_j^2 + q_j^2} + p_j}{2}} - i \sqrt{\frac{\sqrt{p_j^2 + q_j^2} - p_j}{2}} \quad (5)$$

where

$$p_j = 1 + (\kappa_j^2 - n_j^2) \left(\frac{n_0 \sin \theta_0}{n_j^2 + \kappa_j^2} \right)^2, \quad (6)$$

and

$$q_j = -2n_j \kappa_j \left(\frac{n_0 \sin \theta_0}{n_j^2 + \kappa_j^2} \right)^2. \quad (7)$$

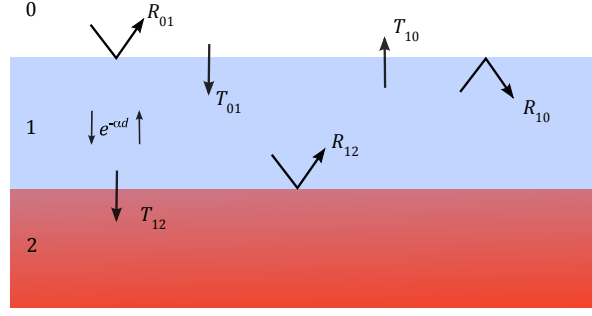


Figure A-1: Graphical representation of the single interface intensity reflectance and transmittance coefficients used to derive R and T .

It will be useful in the following to cast the expressions for R and T in terms of the single-interface field-*amplitude* reflection, ρ_{jk} , and transmission, τ_{jk} , coefficients. which provide the ratio between the incident, reflected, and transmitted parallel-component of \mathcal{E} at an interface of two media with refractive indices \tilde{n}_j and \tilde{n}_k . Specifically [11]:

$$\rho_{jk} = \frac{\eta_j - \eta_k}{\eta_j + \eta_k}, \quad (8)$$

and

$$\tau_{jk} = \frac{2\eta_j}{\eta_j + \eta_k}. \quad (9)$$

Both ρ_{jk} and τ_{jk} are generally complex quantities. The first and second subscripts on both quantities refers to the media on the incident and transmitting side of the interface, respectively.

Referring to Figure A-1, at the interface between media j and k , a fraction R_{jk} of an incident wave's intensity is reflected and a fraction T_{jk} is transmitted. These single-interface intensity coefficients are given in terms of the corresponding amplitude coefficients [11]:

$$R_{jk} = |\rho_{jk}|^2, \quad (10)$$

and

$$T_{jk} = \frac{\Re\{\eta_k\}}{\Re\{\eta_j\}} |\tau_{jk}|^2, \quad (11)$$

where \Re designates the real part of a quantity. The T_{jk} can also be written in terms of ρ_{jk} :

$$T_{jk} = 1 - |\rho_{jk}|^2 + \frac{\Re\{\eta_j^*(\rho_{jk} - \rho_{jk}^*)\}}{\Re\{\eta_j\}} \quad (12)$$

For $\kappa_1 \neq 0$, we must take account of the energy absorption within the sample. Across the sample's thickness, there is a shift in the wave's complex phase equal to

$$\tilde{\phi} = \frac{2\pi\tilde{n}_1}{\lambda} d \cos \theta_1. \quad (13)$$

The imaginary part of $\tilde{\phi}$, which we will denote as α , determines the wave's attenuation while traversing the sample and is given by:

$$\alpha = \frac{4\pi}{\lambda_0} (\kappa_1 a_1 + n_1 b_1). \quad (14)$$

The attenuation factor experienced by a wave over one transit of the sample is $e^{-\alpha d}$, as indicated in Figure A-1.

Finally, the incoherent R and T can be calculated most directly by summing over the path of an imaginary ray experiencing an infinite number of reflections within medium-1. Skipping the details, this produces the following expressions:

$$R = \frac{R_{01} + R_{12}e^{-2\alpha d} (T_{01}T_{10} - R_{01}^2)}{1 - R_{01}R_{12}e^{-2\alpha d}}, \quad (15)$$

and

$$T = \frac{T_{01}T_{12}e^{-\alpha d}}{1 - R_{01}R_{12}e^{-2\alpha d}}. \quad (16)$$

In the case $\kappa_1 = 0$, we have $T_{01} = T_{10} = 1 - R_{01}$ and Equation (1) reduces to the usual expression for R , namely $R = (R_{01} + R_{12} - 2R_{01}R_{12})/(1 - R_{01}R_{12})$.

This page intentionally left blank.

References

- [1] J. M. Ziman, *Principles of the Theory of Solids*, 2nd ed. Cambridge, UK: Cambridge University Press, 1972.
- [2] G. M. Hale and M. R. Query, "Optical Constants of Water in the 200-nm to 200-microm Wavelength Region." *Appl. Opt.*, vol. 12, no. 3, pp. 555–563, 1973.
- [3] S. G. Warren and R. E. Brandt, "Optical constants of ice from the ultraviolet to the microwave: A revised compilation," *J. Geophys. Res. Atmos.*, vol. 113, p. D14220, 2008.
- [4] Y. Sarov, S. Sainov, and V. Marinova, "Refractive index of ferroelectric $\text{Pb}_2\text{ScTaO}_6$ single crystals around the phase transition," *Mater. Sci. Eng. B*, vol. 83, pp. 231–234, 2001.
- [5] M. Zakerhamidi and H. Rahimzadeh, "Order parameters and refractive indices of some cyano-benzoate nematic liquid crystals with high transition temperatures," *J. Mol. Liq.*, vol. 172, pp. 41–45, 2012.
- [6] C. F. Bohren and D. R. Huffman, *Absorption and Scattering of Light by Small Particles*. Weinheim: Wiley-VCH Verlag GmbH, 2004.
- [7] B. Hapke, *Theory of Reflectance and Emittance Spectroscopy*. Cambridge: Cambridge University Press, 1993.
- [8] T. Mooney and R. F. Knacke, "Optical constants of chlorite and serpentine between 2.5 and 50 μm ," *Icarus*, vol. 64, no. 3, pp. 493–502, Dec. 1985.
- [9] M. L. Wenrich and P. R. Christensen, "Optical constants of minerals derived from emission spectroscopy: Application to quartz," *J. Geophys. Res.*, vol. 101, no. B7, pp. 15 921–15 931, Jun. 1996.
- [10] T. D. Glotch and G. R. Rossman, "Mid-infrared reflectance spectra and optical constants of six iron oxide/oxyhydroxide phases," *Icarus*, vol. 204, no. 2, pp. 663–671, Dec. 2009.
- [11] H. A. Macleod, *Thin-Film Optical Filters*, 3rd ed. New York, NY: Taylor & Francis Group, 2001.
- [12] R. Hudson, P. Gerakines, and M. Moore, "Infrared spectra and optical constants of astronomical ices: II. Ethane and ethylene," *Icarus*, vol. 243, pp. 148–157, Nov. 2014.
- [13] A. Einstein, "Strahlungs-Emission und Absorption nach der Quantentheorie," *Dtsch. Phys. Gesellschaft*, 1916.
- [14] M. Šimečková, D. Jacquemart, L. S. Rothman, R. R. Gamache, and A. Goldman, "Einstein A-coefficients and statistical weights for molecular absorption transitions in the HITRAN database," *J. Quant. Spectrosc. Radiat. Transf.*, vol. 98, no. 1, pp. 130–155, Mar. 2006.
- [15] C. Joblin, L. D'Hendrecourt, A. Léger, and D. Défourneau, "Infrared spectroscopy of gas-phase PAH molecules I. Role of the physical environment," *Astron. Astrophys.*, vol. 281, pp. 923–936, 1994.
- [16] H. R. Zelsmann, "Temperature dependence of the optical constants for liquid H_2O and D_2O in the far IR region," *J. Mol. Struct.*, vol. 350, no. 2, pp. 95–114, 1995.
- [17] C. Girardet, J. Humbert, and P. Hoang, "Theoretical approach of the infrared profile of molecular adsorbates on clean surfaces: inhomogeneous broadening," *Chem. Phys.*, vol. 230, no. 1, pp. 67–81, Apr. 1998.
- [18] W. Grundy and B. Schmitt, "The temperature-dependent near-infrared absorption spectrum of hexagonal H_2O ice," *J. Geophys. Res.*, vol. 103, no. E11, pp. 809–822, 1998.
- [19] Y. Wu, F. Meersman, K. Heremans, and Y. Ozaki, "Hybrid two-dimensional correlation infrared study on the temperature- and pressure-induced concentration dynamics and structural variations of poly(N-isopropylacrylamide)," *J. Mol. Struct.*, vol. 799, pp. 134–140, Nov. 2006.
- [20] P. Majewska, M. Rospenk, B. Czarnik-Matusiewicz, A. Kochel, L. Sobczyk, and R. Dbrowski, "Structure and polarized IR spectra of 4-isothiocyanatophenyl 4-heptylbenzoate (7TPB)," *Chem. Phys.*, vol. 354, pp. 186–195, Dec. 2008.

- [21] R. Hudson, M. Moore, and L. Raines, "Ethane ices in the outer Solar System: Spectroscopy and chemistry," *Icarus*, vol. 203, no. 2, pp. 677–680, Oct. 2009.
- [22] C. Marcott, G. M. Story, A. E. Dowrey, J. T. Grothaus, D. C. Oertel, I. Noda, E. Margalith, and L. Nguyen, "Mining the information content buried in infrared and nearinfrared band shapes by temporal, spatial, and other perturbations," *Appl. Spectrosc.*, vol. 63, no. 12, p. 346A, 2009.
- [23] M. M. Bishop, R. S. Chellappa, Z. Liu, D. N. Preston, M. M. Sandstrom, D. M. Dattelbaum, Y. K. Vohra, and N. Velisavljevic, "High pressure-temperature polymorphism of 1,1-diamino-2,2-dinitroethylene," *J. Phys. Conf. Ser.*, vol. 500, p. 052005, 2014.
- [24] H. Ozbek, S. Ustunel, E. Kutlu, and M. Cetinkaya, "A simple method to determine high-accuracy refractive indices of liquid crystals and the temperature behavior of the related optical parameters via high-resolution birefringence data," *J. Mol. Liq.*, vol. 199, pp. 275–286, 2014.
- [25] G. Boer, I. Sokolik, and S. Martin, "Infrared optical constants of aqueous sulfate nitrate ammonium multicomponent tropospheric aerosols from attenuated total reflectance measurements, Part I: Results and analysis of spectral absorbing features," *J. Quant. Spectrosc. Radiat. Transf.*, vol. 108, pp. 17–38, Nov. 2007.
- [26] C. Areal, M. Delgado, R. Bulánek, and K. Frolich, "Combined microcalorimetric and IR spectroscopic study on carbon dioxide adsorption in H-MCM-22," *Appl. Surf. Sci.*, vol. 316, pp. 532–536, Oct. 2014.
- [27] J. R. Schoonover, D. M. Dattelbaum, J. C. Osborn, J. S. Bridgewater, and J. W. Kenney, "Pressure-dependent Fourier transform infrared spectroscopy of a poly (ester urethane)," *Spectrochim. Acta Part A Mol. Biomol. Spectrosc.*, vol. 59, pp. 309–319, Jan. 2003.
- [28] E. D. Emmons, R. G. Kraus, S. S. Duvvuri, J. S. Thompson, and A. M. Covington, "High-pressure infrared absorption spectroscopy of poly(methyl methacrylate)," *J. Polym. Sci. Part B Polym. Phys.*, vol. 45, no. 3, pp. 358–367, Feb. 2007.
- [29] Y. Tsuchida and T. Yagi, "New pressure-induced transformations of silica at room temperature," *Nature*, vol. 347, no. 6290, pp. 267–269, Sep. 1990.
- [30] O. Mishima and H. E. Stanley, "Decompression-induced melting of ice IV and the liquidliquid transition in water," *Nature*, vol. 392, no. 6672, pp. 164–168, Mar. 1998.
- [31] Q. Williams and R. Jeanloz, "Spectroscopic Evidence for Pressure-Induced Coordination Changes in Silicate Glasses and Melts," *Science*, vol. 239, no. 4842, pp. 902–905, Feb. 1988.
- [32] M. Pravica, M. Galley, E. Kim, P. Weck, and Z. Liu, "A far- and mid-infrared study of HMX (octahydro-1,3,5,7-tetranitro-1,3,5,7-tetrazocine) under high pressure," *Chem. Phys. Lett.*, vol. 500, no. 1-3, pp. 28–34, Nov. 2010.
- [33] F. Goetz, T. B. Brill, and J. R. Ferraro, "Pressure dependence of the Raman and infrared spectra of α -, β -, γ -, and δ -octahydro-1,3,5,7-tetranitro-1,3,5,7-tetrazocine," *J. Phys. Chem.*, vol. 82, no. 17, pp. 1912–1917, Aug. 1978.
- [34] G. D. Saraiva, M. Maczka, P. T. C. Freire, J. Mendes Filho, F. E. A. Melo, J. Hanuza, Y. Morioka, and A. G. Souza Filho, "Pressure-induced irreversible phase transition in KSc(MoO₄)," *Phys. Rev. B*, vol. 67, no. 22, p. 224108, Jun. 2003.
- [35] Z. A. Dreger and Y. M. Gupta, "Phase Diagram of Hexahydro-1,3,5-trinitro-1,3,5-triazine Crystals at High Pressures and Temperatures," *J. Phys. Chem. A*, vol. 114, no. 31, pp. 8099–8105, Aug. 2010.
- [36] C. Joblin, P. Boissel, a. Leger, L. D'Hendecourt, and D. Defourneau, "Infrared spectroscopy of gas-phase PAH molecules II. Role of the temperature," *Astron. Astrophys.*, vol. 299, pp. 835–846, 1995.

- [37] A. Politano, G. Chiarello, G. Benedek, E. Chulkov, and P. Echenique, "Vibrational spectroscopy and theory of alkali metal adsorption and co-adsorption on single-crystal surfaces," *Surf. Sci. Rep.*, vol. 68, no. 3-4, pp. 305–389, Nov. 2013.
- [38] R. Hudson, R. Ferrante, and M. Moore, "Infrared spectra and optical constants of astronomical ices: I. Amorphous and crystalline acetylene," *Icarus*, vol. 228, pp. 276–287, Jan. 2014.
- [39] S. T. Martin, D. Salcedo, L. T. Molina, and M. J. Molina, "Phase Transformations of Micron-Sized H₂SO₄/H₂O Particles Studied by Infrared Spectroscopy," *J. Phys. Chem. B*, vol. 101, no. 27, pp. 5307–5313, Jul. 1997.
- [40] L. Colangeli, V. Mennella, and E. Bussolleti, "Temperature dependence of infrared bands produced by polycyclic aromatic hydrocarbons," *Astrophys. J.*, vol. 385, p. 577, Feb. 1992.
- [41] H. Foerstendorf, N. Jordan, and K. Heim, "Probing the surface speciation of uranium (VI) on iron (hydr)oxides by in situ ATR FT-IR spectroscopy," *J. Colloid Interface Sci.*, vol. 416, pp. 133–138, Feb. 2014.
- [42] E. Carrasco, A. Aumer, M. A. Brown, R. Dowler, I. Palacio, S. Song, and M. Sterrer, "Infrared spectra of high coverage CO adsorption structures on Pt(111)," *Surf. Sci.*, vol. 604, no. 15-16, pp. 1320–1325, Aug. 2010.
- [43] G. Spoto, E. N. Gribov, G. Ricchiardi, A. Damin, D. Scarano, S. Bordiga, C. Lamberti, and A. Zecchina, "Carbon monoxide MgO from dispersed solids to single crystals: A review and new advances," *Prog. Surf. Sci.*, vol. 76, no. 3-5, pp. 71–146, 2004.
- [44] T. Fornaro, J. R. Brucato, E. Pace, M. C. Guidi, S. Branciamore, and A. Pucci, "Infrared spectral investigations of UV irradiated nucleobases adsorbed on mineral surfaces," *Icarus*, vol. 226, no. 1, pp. 1068–1085, 2013.
- [45] H. Foerstendorf, K. Heim, and A. Rossberg, "The complexation of uranium(VI) and atmospherically derived CO₂ at the ferrihydrite-water interface probed by time-resolved vibrational spectroscopy," *J. Colloid Interface Sci.*, vol. 377, no. 1, pp. 299–306, Jul. 2012.
- [46] J. D. Fox, "Infrared vibrational spectra of tert-butyl halides in low-aluminum H-Y Faujasite: Vibrational excitation exchange and other effects of guest-host interactions," *Chem. Phys.*, vol. 325, no. 2-3, pp. 265–277, Jun. 2006.
- [47] J. Chowdhury, J. Sarkar, R. De, M. Ghosh, and G. Talapatra, "Adsorption of 2-amino-6-methylbenzothiazole on colloidal silver particles: Quantum chemical calculations and surface enhanced Raman scattering study," *Chem. Phys.*, vol. 330, no. 1-2, pp. 172–183, Nov. 2006.
- [48] H. Zorgati, C. Ramseyer, and C. Girardet, "Heterogeneous against homogeneous spectral response of polar molecules adsorbed on a real surface," *Chem. Phys.*, vol. 362, no. 1-2, pp. 41–57, Jul. 2009.
- [49] M. Moskovits, "Surface selection rules," *J. Chem. Phys.*, vol. 77, no. 9, p. 4408, 1982.
- [50] J. Creighton, "Surface raman electromagnetic enhancement factors for molecules at the surface of small isolated metal spheres: The determination of adsorbate orientation from sers relative intensities," *Surf. Sci.*, vol. 124, no. 1, pp. 209–219, Jan. 1983.
- [51] T. Yamada, K. Shirasaka, A. Takano, and M. Kawai, "Adsorption of cytosine, thymine, guanine and adenine on Cu(1 1 0) studied by infrared reflection absorption spectroscopy," *Surf. Sci.*, vol. 561, no. 2-3, pp. 233–247, 2004.
- [52] E. Mateo-Martí, C. Briones, C. Rogero, C. Gomez-Navarro, C. Methivier, C. Pradier, and J. Martín-Gago, "Nucleic acid interactions with pyrite surfaces," *Chem. Phys.*, vol. 352, no. 1-3, pp. 11–18, Sep. 2008.
- [53] A. Lopez, T. Heller, T. Bitzer, and N. V. Richardson, "A vibrational study of the adsorption of glycine on clean and Na modified Si-21 surfaces," *Chem. Phys.*, vol. 277, no. 1, pp. 1–8, Mar. 2002.

- [54] F. Boccuzzi, A. Chiorino, and E. Guglielminotti, "Effects of structural defects and alloying on the FTIR spectra of CO adsorbed on Pt/ZnO," *Surf. Sci.*, vol. 368, no. 1-3, pp. 264–269, Dec. 1996.
- [55] J. D. Fox and A. Meenakshi, "Effects of tert-butyl halide molecular siting in crystalline NaX faujasite on the infrared vibrational spectra," *J. Phys. Chem. B*, vol. 109, no. 20, pp. 9917–26, May 2005.
- [56] A. Garnier, S. Sall, F. Garin, M. Chetcuti, and C. Petit, "Site effects in the adsorption of carbon monoxide on real 1.8nm Pt nanoparticles: An Infrared investigation in time and temperature," *J. Mol. Catal. A Chem.*, vol. 373, pp. 127–134, Jul. 2013.
- [57] C. D. Zeinalipour-Yazdi, D. J. Willock, L. Thomas, K. Wilson, and A. F. Lee, "CO adsorption over Pd nanoparticles: A general framework for IR simulations on nanoparticles," *Surf. Sci.*, Jul. 2015.
- [58] M. Buchholz, M. Xu, H. Noei, P. Weidler, A. Nefedov, K. Fink, Y. Wang, and C. Wöll, "Interaction of carboxylic acids with rutile TiO₂(110): IR-investigations of terephthalic and benzoic acid adsorbed on a single crystal substrate," *Surf. Sci.*, Aug. 2015.
- [59] Y. Takeshita, E. Becker, S. Sakata, T. Miwa, and T. Sawada, "States of water absorbed in water-borne urethane/epoxy coatings," *Polymer*, vol. 55, no. 10, pp. 2505–2513, May 2014.
- [60] M. Van Thiel, E. D. Becker, and G. C. Pimentel, "Infrared Studies of Hydrogen Bonding of Water by the Matrix Isolation Technique," *J. Chem. Phys.*, vol. 27, no. 2, p. 486, Aug. 1957.
- [61] K. Buijs and G. R. Choppin, "Near-Infrared Studies of the Structure of Water. I. Pure Water," *J. Chem. Phys.*, vol. 39, no. 8, p. 2035, Jun. 1963.
- [62] J. Tennyson, P. F. Bernath, L. R. Brown, A. Campargue, A. G. Császár, L. Daumont, R. R. Gamache, J. T. Hodges, O. V. Naumenko, O. L. Polyansky, L. S. Rothman, A. C. Vandaele, N. F. Zobov, A. R. Al Derzi, C. Fábri, A. Z. Fazliev, T. Furtenbacher, I. E. Gordon, L. Lodi, and I. I. Mizus, "IUPAC critical evaluation of the rotational-vibrational spectra of water vapor, Part III: Energy levels and transition wavenumbers for H₂¹⁶O," *J. Quant. Spectrosc. Radiat. Transf.*, vol. 117, pp. 29–58, 2013.
- [63] D. Eisenberg and W. Kauzmann, *The structure and properties of water*. London: Oxford University Press, 1969.
- [64] J.-J. Max and C. Chapados, "Isotope effects in liquid water by infrared spectroscopy. III. H₂O and D₂O spectra from 6000 to 0 cm⁻¹," *J. Chem. Phys.*, vol. 131, no. 18, p. 184505, Nov. 2009.
- [65] N. Kitadai, T. Sawai, R. Tonoue, S. Nakashima, M. Katsura, and K. Fukushi, "Effects of Ions on the OH Stretching Band of Water as Revealed by ATR-IR Spectroscopy," *J. Solution Chem.*, vol. 43, no. 6, pp. 1055–1077, Jun. 2014.
- [66] C. Sammon, C. Deng, and J. Yarwood, "Polymerwater interactions. Origin of perturbed infrared intensities of water in polymeric systems," *Polymer*, vol. 44, no. 9, pp. 2669–2677, Apr. 2003.
- [67] R. Mastrapa, M. Bernstein, S. Sandford, T. Roush, D. Cruikshank, and C. Ore, "Optical constants of amorphous and crystalline H₂O-ice in the near infrared from 1.1 to 2.6 μm," *Icarus*, vol. 197, no. 1, pp. 307–320, Sep. 2008.
- [68] R. M. Mastrapa, S. a. Sandford, T. L. Roush, D. P. Cruikshank, and C. M. Dalle Ore, "Optical Constants of Amorphous and Crystalline H₂O-Ice: 2.5-22 μm (4000-455 cm⁻¹) Optical Constants of H₂O-Ice," *Astrophys. J.*, vol. 701, no. 2, pp. 1347–1356, Aug. 2009.
- [69] R. E. Milliken and J. F. Mustard, "Quantifying absolute water content of minerals using near-infrared reflectance spectroscopy," *J. Geophys. Res.*, vol. 110, no. E12, pp. 1–25, 2005.
- [70] J. L. Bishop, "Infrared Spectroscopic Analyses on the Nature of Water in Montmorillonite," *Clays Clay Miner.*, vol. 42, no. 6, pp. 702–716, 1994.

- [71] J. D. Russell and V. C. Farmer, "Infra-Red Spectroscopic Study of the Dehydration of Montmorillonite and Saponite," *Clay Miner.*, vol. 5, no. 32, pp. 443–464, 1964.
- [72] G. Sposito, R. Prost, and J.-P. Gaultier, "Infrared Spectroscopic Study of Adsorbed Water on Reduced-Charge Na/Li-Montmorillonites," *Clays Clay Miner.*, vol. 31, no. 1, pp. 9–16, 1983.
- [73] C. T. Johnston, G. Sposito, and C. Erickson, "Vibrational Probe Studies of Water Interactions with Montmorillonite," *Clays Clay Miner.*, vol. 40, no. 6, pp. 722–730, 1992.
- [74] F. Cariatì, L. Erre, G. Micera, P. Piu, and C. Gessa, "Polarization of Water Molecules in Phyllosilicates in Relation to Exchange Cations as Studied by near Infrared Spectroscopy," *Clays Clay Miner.*, vol. 31, no. 2, pp. 155–157, 1983.
- [75] —, "Effects of Layer Charge on the Near-Infrared Spectra of Water Molecules in Smectites and Vermiculites," *Clays Clay Miner.*, vol. 31, no. 6, pp. 447–449, 1983.
- [76] J. A. Hockey and B. A. Pethica, "Surface hydration of silicas," *Trans. Faraday Soc.*, vol. 57, p. 2247, 1961.
- [77] J. Anderson and K. Wickersheim, "Near infrared characterization of water and hydroxyl groups on silica surfaces," *Surf. Sci.*, vol. 2, pp. 252–260, Jan. 1964.
- [78] T. W. Dijkstra, R. Duchateau, R. A. van Santen, A. Meetsma, and G. P. A. Yap, "Silsequioxane Models for Geminal Silica Surface Silanol Sites. A Spectroscopic Investigation of Different Types of Silanols," *J. Am. Chem. Soc.*, vol. 124, no. 33, pp. 9856–9864, Aug. 2002.
- [79] K. Langer and O. W. Florke, "Near infrared absorption spectra (4000-9000 1/cm) of opals and the role of water in these $\text{SiO}_2(\text{nH}_2\text{O})$ minerals," *Fortschritte der Mineral.*, vol. 52, p. 17, 1974.
- [80] M. Rice, E. Cloutis, J. Bell, D. Bish, B. Horgan, S. Mertzman, M. Craig, R. Renaut, B. Gautason, and B. Mountain, "Reflectance spectra diversity of silica-rich materials: Sensitivity to environment and implications for detections on Mars," *Icarus*, vol. 223, no. 1, pp. 499–533, Mar. 2013.
- [81] Y. Maeda, M. Ide, and H. Kitano, "Vibrational spectroscopic study on the structure of water in polymer systems," *J. Mol. Liq.*, vol. 80, no. 2-3, pp. 149–163, May 1999.
- [82] Z. Ping, Q. Nguyen, S. Chen, J. Zhou, and Y. Ding, "States of water in different hydrophilic polymers DSC and FTIR studies," *Polymer*, vol. 42, no. 20, pp. 8461–8467, Sep. 2001.
- [83] G. G. Zundel, *Hydration and intermolecular interactions*. New York: Academic Press, 1969.
- [84] A. Lasagabáster, M. J. Abad, L. Barral, A. Ares, and R. Bouza, "Application of FTIR spectroscopy to determine transport properties and waterpolymer interactions in polypropylene (PP)/poly(ethylene-co-vinyl alcohol) (EVOH) blend films: Effect of poly(ethylene-co-vinyl alcohol) content and water activity," *Polymer*, vol. 50, no. 13, pp. 2981–2989, Jun. 2009.
- [85] D. Cava, L. Cabedo, E. Gimenez, R. Gavara, and J. Lagaron, "The effect of ethylene content on the interaction between ethylenevinyl alcohol copolymers and water: (I) Application of FT-IR spectroscopy to determine transport properties and interactions in food packaging films," *Polym. Test.*, vol. 25, no. 2, pp. 254–261, Apr. 2006.
- [86] S. Cotugno, D. Larobina, G. Mensitieri, P. Musto, and G. Ragosta, "A novel spectroscopic approach to investigate transport processes in polymers: the case of water epoxy system," *Polymer*, vol. 42, no. 15, pp. 6431–6438, Jul. 2001.
- [87] M. Laporta, M. Pegoraro, and L. Zanderighi, "Perfluorosulfonated membrane (Nafion): FT-IR study of the state of water with increasing humidity," *Phys. Chem. Chem. Phys.*, vol. 1, no. 19, pp. 4619–4628, 1999.

- [88] P. Musto, G. Mensitieri, M. Lavorgna, G. Scarinzi, and G. Scherillo, "Combining gravimetric and vibrational spectroscopy measurements to quantify first- and second-shell hydration layers in polyimides with different molecular architectures." *J. Phys. Chem. B*, vol. 116, no. 4, pp. 1209–20, Feb. 2012.
- [89] J. Mijović and H. Zhang, "Local Dynamics and Molecular Origin of Polymer Network Water Interactions as Studied by Broadband Dielectric Relaxation Spectroscopy, FTIR, and Molecular Simulations," *Macromolecules*, vol. 36, no. 4, pp. 1279–1288, Feb. 2003.
- [90] H. X. Yang, M. Sun, and P. Zhou, "Investigation of water diffusion in poly(3-hydroxybutyrate-co-3-hydroxyhexanoate) by generalized two-dimensional correlation ATR-FTIR spectroscopy," *Polymer*, vol. 50, no. 6, pp. 1533–1540, 2009.
- [91] C. Frondel, "Structural hydroxyl in chalcedony (type B quartz)." *Am. Mineral.*, vol. 67, no. 11-12, pp. 1248–1257, 1982.
- [92] L. Philippe, C. Sammon, S. B. Lyon, and J. Yarwood, "An FTIR/ATR in situ study of sorption and transport in corrosion protective organic coatings," *Prog. Org. Coatings*, vol. 49, no. 4, pp. 302–314, May 2004.
- [93] J. R. Schoonover, W. P. Steckle, J. D. Cox, C. T. Johnston, Y. Wang, A. M. Gillikin, and R. A. Palmer, "Humidity-dependent dynamic infrared linear dichroism study of a poly(ester urethane)," *Spectrochim. Acta Part A Mol. Biomol. Spectrosc.*, vol. 67, no. 1, pp. 208–213, May 2007.
- [94] L.-M. Döppers, C. Sammon, C. Breen, and J. Yarwood, "FTIR-ATR studies of the sorption and diffusion of acetone/water mixtures in poly(vinyl alcohol)," *Polymer*, vol. 47, no. 8, pp. 2714–2722, Apr. 2006.
- [95] N. S. Schneider, J. L. Illinger, and F. E. Karasz, "The interaction of water with polyurethanes containing block copolymer soft segments," *J. Appl. Polym. Sci.*, vol. 47, no. 8, pp. 1419–1425, Feb. 1993.
- [96] P. Pissis, L. Apekis, C. Christodoulides, M. Niaounakis, A. Kyritsis, and J. Nedbal, "Water effects in polyurethane block copolymers," *J. Polym. Sci. Part B Polym. Phys.*, vol. 34, no. 9, pp. 1529–1539, Jul. 1996.
- [97] A. Wang and Y. Zhou, "Experimental comparison of the pathways and rates of the dehydration of Al-, Fe-, Mg- and Ca-sulfates under Mars relevant conditions," *Icarus*, vol. 234, pp. 162–173, May 2014.
- [98] G. Openhaim and E. Grushka, "Temperature-dependent refractive index issues using a UVvisible detector in high-performance liquid chromatography," *J. Chromatogr. A*, vol. 942, no. 1-2, pp. 63–71, Jan. 2002.
- [99] R. J. Riobóo, M. Philipp, M. a. Ramos, and J. K. Krüger, "Concentration and temperature dependence of the refractive index of ethanol-water mixtures: Influence of intermolecular interactions," *Eur. Phys. J. E*, vol. 30, no. 1, pp. 19–26, Sep. 2009.
- [100] I. Bratu, R. Grecu, R. Constantinescu, and T. Iliescu, "Molecular relaxation processes of 2-bromopropane in solutions from IR $\nu(\text{CBr})$ band shape analysis," *Spectrochim. Acta Part A Mol. Biomol. Spectrosc.*, vol. 54, no. 3, pp. 501–506, Mar. 1998.
- [101] D. Yamini, V. Sasirekha, and V. Ramakrishnan, "Raman spectral studies on 2-hydroxyacetophenone in binary liquid mixtures," *Vib. Spectrosc.*, vol. 61, pp. 30–37, Jul. 2012.
- [102] N. Tekin, C. Uyank, and S. K. Beyaz, "The Effects of Organic Solvents on the Frequency of C=O Stretching Vibration in Isophorone, 4-oxo-isophorone, and 2,6,6-trimethyl-4,4-(ethylenedioxy)cyclohex-2-en-1-one," *J. Appl. Spectrosc.*, vol. 81, no. 4, pp. 711–718, Sep. 2014.
- [103] R. Nyquist, R. Streck, and G. Jeschek, "NMR and IR spectra-structure correlations for carbonyl containing compounds in various solvents," *J. Mol. Struct.*, vol. 377, no. 2, pp. 113–128, Mar. 1996.
- [104] F. Khan and P. Sivagurunathan, "Infrared studies on hydrogen bonding interaction between acrylic esters with 1-dodeconal and phenol in carbon tetrachloride," *Phys. Chem. Liq.*, vol. 46, no. 5, pp. 504–509, Oct. 2008.

- [105] Q. Liu, Y. Liu, H. Zhang, and Z. Wen, "Solvent effects on infrared spectroscopy of 17 β -hydroxy-17-methyl-2-oxa-5 α -androstan-3-one in single solvents," *Spectrochim. Acta Part A Mol. Biomol. Spectrosc.*, vol. 65, no. 1, pp. 164–168, Sep. 2006.
- [106] B. Hernández, J. M. Gavira-Vallejo, R. Navarro, and A. Hernanz, "Splitting of infrared bands of mononucleotides in aqueous solution," *J. Mol. Struct.*, vol. 565-566, pp. 259–263, 2001.
- [107] A. Stolov, W. Herrebout, and B. van der Veken, "Solvent effect on vibrational frequencies: cryosolution experiments and density functional calculations," *J. Mol. Struct.*, vol. 480-481, pp. 499–503, May 1999.
- [108] A. Zimniak, I. Oszczapowicz, A. Sikora, and I. Wawer, "Solvent-dependent conformational transitions in deacetylcephalothin investigated by ^1H NMR and IR," *J. Mol. Struct.*, vol. 443, no. 1-3, pp. 115–121, Feb. 1998.
- [109] J. S. Walker and C. A. Vause, "Reappearing Phases," *Sci. Am.*, vol. 256, no. 5, pp. 98–105, May 1987.
- [110] A. Le Bras and S. Erard, "Reflectance spectra of regolith analogs in the mid-infrared: Effects of grain size," *Planet. Space Sci.*, vol. 51, no. 4-5, pp. 281–294, 2003.
- [111] B. H. Horgan, E. A. Cloutis, P. Mann, and J. F. Bell, "Near-infrared spectra of ferrous mineral mixtures and methods for their identification in planetary surface spectra," *Icarus*, vol. 234, pp. 132–154, May 2014.
- [112] T. L. Myers, C. S. Brauer, Y.-F. Su, T. a. Blake, T. J. Johnson, and R. L. Richardson, "The influence of particle size on infrared reflectance spectra," in *Proc. SPIE*, vol. 9088, 2014, p. 908809.
- [113] F. Mancarella, V. Orofino, A. Blanco, M. D'Elia, and S. Fonti, "The role of particle size in the laboratory reflectance spectra of pyroxenes: The case of the 670-nm minor feature," *Planet. Space Sci.*, May 2015.
- [114] Y.-F. Su, T. L. Myers, C. S. Brauer, T. a. Blake, B. M. Forland, J. E. Szecsody, and T. J. Johnson, "Infrared reflectance spectra: effects of particle size, provenance and preparation," in *Proc. SPIE*, vol. 9253, 2014, p. 925304.
- [115] V. E. Hamilton, R. V. Morris, J. E. Gruener, and S. a. Mertzman, "Visible, near-infrared, and middle infrared spectroscopy of altered basaltic tephra: Spectral signatures of phyllosilicates, sulfates, and other aqueous alteration products with application to the mineralogy of the Columbia Hills of Gusev Crater, Mars," *J. Geophys. Res. E Planets*, vol. 113, no. 12, pp. 1–30, 2008.
- [116] J. E. Moersch and P. R. Christensen, "Thermal emission from particulate surfaces: A comparison of scattering models with measured spectra," *J. Geophys. Res.*, vol. 100, no. E4, pp. 7465–7477, 1995.
- [117] G. R. Hunt and L. M. Logan, "Variation of single particle mid-infrared emission spectrum with particle size," *Appl. Opt.*, vol. 11, no. 1, pp. 142–7, Jan. 1972.
- [118] M. Lane and P. R. Christensen, "Thermal Infrared Emission Spectroscopy of Salt Minerals Predicted for Mars," *Icarus*, vol. 135, no. 2, pp. 528–536, Oct. 1998.
- [119] M. D. Lane, "Midinfrared optical constants of calcite and their relationship to particle size effects in thermal emission spectra of granular calcite," *J. Geophys. Res.*, vol. 104, no. E6, pp. 14 099–14 108, 1999.
- [120] J. Mustard and J. Hays, "Effects of Hyperfine Particles on Reflectance Spectra from 0.3 to 25 μm ," *Icarus*, vol. 125, no. 1, pp. 145–163, Jan. 1997.
- [121] L. Moroz, A. Basilevsky, T. Hiroi, S. Rout, D. Baither, C. van der Bogert, O. Yakovlev, A. Fisenko, L. Semjonova, V. Rusakov, D. Khramov, N. Zinovieva, G. Arnold, and C. Pieters, "Spectral properties of simulated impact glasses produced from martian soil analogue JSC Mars-1," *Icarus*, vol. 202, no. 1, pp. 336–353, Jul. 2009.
- [122] C. Cooper and J. Mustard, "Effects of Very Fine Particle Size on Reflectance Spectra of Smectite and Palagonitic Soil," *Icarus*, vol. 142, no. 2, pp. 557–570, Dec. 1999.

- [123] B. L. Cooper, "Midinfrared spectral features of rocks and their powders," *J. Geophys. Res.*, vol. 107, no. E4, pp. 1–1 – 1–17, 2002.
- [124] M. Papini, "Study of the radiative properties of powdered and fibrous polymers," *Vib. Spectrosc.*, vol. 11, no. 1, pp. 61–68, Mar. 1996.
- [125] S. Fonti, S. Montanaro, R. Politi, A. Blanco, a. C. Marra, G. a. Marzo, and V. Orofino, "Infrared reflectance spectra of particulate mixtures," *J. Geophys. Res.*, vol. 115, no. E6, Jun. 2010, E06003.
- [126] J. R. Johnson, P. R. Christensen, and P. G. Lucey, "Dust coatings on basaltic rocks and implications for thermal infrared spectroscopy of Mars," *J. Geophys. Res.*, vol. 107, no. E6, 2002.
- [127] P. G. Lucey, "Model near-infrared optical constants of olivine and pyroxene as a function of iron content," *J. Geophys. Res.*, vol. 103, no. E1, p. 1703, Jan. 1998.
- [128] J. Salisbury and A. Wald, "The role of volume scattering in reducing spectral contrast of reststrahlen bands in spectra of powdered minerals," *Icarus*, vol. 96, no. 1, pp. 121–128, Mar. 1992.
- [129] A. E. Wald and J. W. Salisbury, "Thermal infrared directional emissivity of powdered quartz," *J. Geophys. Res.*, vol. 100, no. B12, p. 24665, 1995.
- [130] A. Jurewicz, V. Orofino, A. C. Marra, and A. Blanco, "Optical constants of powdered limestone obtained by taking into account the grain shapes: Applicability to Martian studies," *Astron. Astrophys.*, vol. 410, no. 3, pp. 1055–1062, Nov. 2003.
- [131] V. Orofino, A. Blanco, S. Fonti, R. Proce, and A. Rotundi, "The infrared optical constants of limestone particles and implications for the search of carbonates on Mars," *Planet. Space Sci.*, vol. 46, no. 11-12, pp. 1659–1669, Nov. 1998.
- [132] L. Long, M. Querry, R. Bell, and R. Alexander, "Optical properties of calcite and gypsum in crystalline and powdered form in the infrared and far-infrared," *Infrared Phys.*, vol. 34, no. 2, pp. 191–201, Apr. 1993.
- [133] V. P. Tishkovets, E. V. Petrova, and M. I. Mishchenko, "Scattering of electromagnetic waves by ensembles of particles and discrete random media," *J. Quant. Spectrosc. Radiat. Transf.*, vol. 112, no. 13, pp. 2095–2127, 2011.
- [134] R. K. Vincent and G. R. Hunt, "Infrared reflectance from mat surfaces," *Appl. Opt.*, vol. 7, no. 1, pp. 53–9, Jan. 1968.
- [135] G. R. Hunt and R. K. Vincent, "The Behavior of Spectral Features in the Infrared Emission from Particulate Surfaces of Various Grain Sizes," *J. Geophys. Res.*, vol. 73, no. 18, pp. 6039–6046, 1968.
- [136] M. J. Harris, E. K. H. Salje, and B. K. Guttler, "An infrared spectroscopic study of the internal modes of sodium nitrate: implications for the structural phase transition," *J. Phys. Condens. Matter*, vol. 2, no. 25, p. 5517, 1990.
- [137] Y. Okada and A. Kokhanovsky, "Light scattering and absorption by densely packed groups of spherical particles," *J. Quant. Spectrosc. Radiat. Transf.*, vol. 110, no. 11, pp. 902–917, Jul. 2009.
- [138] M. D. Kraft, "Effects of pure silica coatings on thermal emission spectra of basaltic rocks: Considerations for Martian surface mineralogy," *Geophys. Res. Lett.*, vol. 30, no. 24, p. 2288, 2003.
- [139] K. Stack and R. Milliken, "Modeling near-infrared reflectance spectra of clay and sulfate mixtures and implications for Mars," *Icarus*, vol. 250, pp. 332–356, Apr. 2015.
- [140] T. Hiroi and C. M. Pieters, "Estimation of grain sizes and mixing ratios of fine powder mixtures of common geologic minerals," *J. Geophys. Res.*, vol. 99, no. E5, pp. 10 867–10 879, 1994.

- [141] F. Poulet and S. Erard, "Nonlinear spectral mixing: Quantitative analysis of laboratory mineral mixtures," *J. Geophys. Res.*, vol. 109, no. E2, p. E02009, 2004.
- [142] M. S. West, R. G. Resmini, and K. Manville, "Quantification of Constituents in Areal and Intimate Binary Mixtures of Particulate Materials," *Proc. SPIE*, vol. 8040, no. 703, pp. 1–12, 2011.
- [143] R. G. Resmini, R. S. Rand, D. W. Allen, and C. J. Deloye, "An analysis of the nonlinear spectral mixing of didymium and soda-lime glass beads using hyperspectral imagery (HSI) microscopy," *Proc. SPIE*, vol. 9088, p. 90880Z, Jun. 2014.
- [144] Y. Shkuratov, L. Starukhina, H. Hoffmann, and G. Arnold, "A Model of Spectral Albedo of Particulate Surfaces : Implications for Optical Properties of the Moon," *Icarus*, vol. 137, pp. 235–246, 1999.
- [145] M. I. Mishchenko, "Multiple scattering, radiative transfer, and weak localization in discrete random media: Unified microphysical approach," *Rev. Geophys.*, vol. 46, no. 2, pp. 1–33, Apr. 2008.
- [146] B. Teolis, M. Loeffler, U. Raut, M. Famá, and R. Baragiola, "Infrared reflectance spectroscopy on thin films: Interference effects," *Icarus*, vol. 190, no. 1, pp. 274–279, Sep. 2007.
- [147] E. N. Brown and D. M. Dattelbaum, "The role of crystalline phase on fracture and microstructure evolution of polytetrafluoroethylene (PTFE)," *Polymer (Guildf.)*, vol. 46, no. 9, pp. 3056–3068, Apr. 2005.
- [148] Y. A. Eremin, J. C. Stover, and N. V. Grishina, "Discrete sources method for light scattering analysis from 3D asymmetrical features on a substrate," *J. Quant. Spectrosc. Radiat. Transf.*, vol. 70, no. 4-6, pp. 421–431, Aug. 2001.
- [149] J. Hellmers and T. Wriedt, "Influence of particle shape models on T-matrix light scattering simulation," *J. Quant. Spectrosc. Radiat. Transf.*, vol. 89, no. 1-4, pp. 97–110, Nov. 2004.
- [150] P. Yang, Q. Feng, G. Hong, G. Kattawar, W. Wliscombe, M. I. Mischenko, O. Dubovik, I. Laszlo, and I. Sokolik, "Modeling of the scattering and radiative properties of nonspherical dust-like aerosols," *J. Aerosol Sci.*, vol. 38, no. 10, pp. 995–1014, Oct. 2007.
- [151] Z. Meng, P. Yang, G. W. Kattawar, L. Bi, K. Liou, and I. Laszlo, "Single-scattering properties of tri-axial ellipsoidal mineral dust aerosols: A database for application to radiative transfer calculations," *J. Aerosol Sci.*, vol. 41, no. 5, pp. 501–512, May 2010.
- [152] F. Gruy, "Relationship between the morphology and the light scattering cross section of optically soft aggregates," *J. Quant. Spectrosc. Radiat. Transf.*, vol. 112, pp. 2609–2618, Jul. 2011.
- [153] M. Kahnert, T. Nousiainen, and P. Mauno, "On the impact of non-sphericity and small-scale surface roughness on the optical properties of hematite aerosols," *J. Quant. Spectrosc. Radiat. Transf.*, vol. 112, pp. 1815–1824, Jan. 2011.
- [154] T. Nousiainen, M. Kahnert, and H. Lindqvist, "Can particle shape information be retrieved from light-scattering observations using spheroidal model particles?" *J. Quant. Spectrosc. Radiat. Transf.*, vol. 112, no. 13, pp. 2213–2225, Sep. 2011.
- [155] E. V. Petrova and V. P. Tishkovets, "Light scattering by aggregates of varying porosity and the opposition phenomena observed in the low-albedo particulate media," *J. Quant. Spectrosc. Radiat. Transf.*, vol. 112, no. 13, pp. 2226–2233, Jan. 2011.
- [156] R. Vilaplana, R. Luna, and D. Guirado, "The shape influence on the overall single scattering properties of a sample in random orientation," *J. Quant. Spectrosc. Radiat. Transf.*, vol. 112, no. 11, pp. 1838–1847, Jan. 2011.
- [157] C. M. Sorensen, "Q-space analysis of scattering by particles: A review," *J. Quant. Spectrosc. Radiat. Transf.*, vol. 131, pp. 3–12, Dec. 2013.

- [158] E. Zubko, K. Muinonen, O. Muñoz, T. Nousiainen, Y. Shkuratov, W. Sun, and G. Videen, “Light scattering by feldspar particles: Comparison of model agglomerate debris particles with laboratory samples,” *J. Quant. Spectrosc. Radiat. Transf.*, vol. 131, pp. 175–187, Dec. 2013.
- [159] E. Zubko, Y. Shkuratov, and G. Videen, “Effect of morphology on light scattering by agglomerates,” *J. Quant. Spectrosc. Radiat. Transf.*, vol. 150, pp. 42–54, Jan. 2015.
- [160] L. Bi and P. Yang, “Accurate simulation of the optical properties of atmospheric ice crystals with the invariant imbedding T-matrix method,” *J. Quant. Spectrosc. Radiat. Transf.*, vol. 138, pp. 17–35, 2014.
- [161] A. Doicu, Y. Eremin, D. S. Efremenko, and T. Trautmann, “Methods with discrete sources for electromagnetic scattering by large axisymmetric particles with extreme geometries,” *J. Quant. Spectrosc. Radiat. Transf.*, vol. 164, pp. 137–146, Oct. 2015.
- [162] Y. Wu, T. Cheng, L. Zheng, H. Chen, and H. Xu, “Single scattering properties of semi-embedded soot morphologies with intersecting and non-intersecting surfaces of absorbing spheres and non-absorbing host,” *J. Quant. Spectrosc. Radiat. Transf.*, vol. 157, pp. 1–13, May 2015.
- [163] O. Kempainen, T. Nousiainen, and H. Lindqvist, “The impact of surface roughness on scattering by realistically shaped wavelength-scale dust particles,” *J. Quant. Spectrosc. Radiat. Transf.*, vol. 150, pp. 55–67, Jan. 2015.
- [164] P. D. Kleiber, V. H. Grassian, M. a. Young, and P. K. Hudson, “T -matrix studies of aerosol particle shape effects on IR resonance spectral line profiles and comparison with an experiment,” *J. Geophys. Res.*, vol. 114, no. D21, pp. 1–10, Nov. 2009.
- [165] N. Kiomarsipour, R. Shoja Razavi, K. Ghani, and M. Kioumarsipour, “Evaluation of shape and size effects on optical properties of ZnO pigment,” *Appl. Surf. Sci.*, vol. 270, pp. 33–38, 2013.
- [166] M. I. Mishchenko, “Bidirectional reflectance of flat, optically thick particulate layers: an efficient radiative transfer solution and applications to snow and soil surfaces,” *J. Quant. Spectrosc. Radiat. Transf.*, vol. 63, no. 2-6, pp. 409–432, Sep. 1999.
- [167] L. E. Kirkland, K. C. Herr, and P. M. Adams, “Infrared stealthy surfaces: Why TES and THEMIS may miss some substantial mineral deposits on Mars and implications for remote sensing of planetary surfaces,” *J. Geophys. Res.*, vol. 108, no. E12, p. 5137, 2003.
- [168] M. M. Osterloo, V. E. Hamilton, and F. S. Anderson, “A laboratory study of the effects of roughness on the thermal infrared spectra of rock surfaces,” *Icarus*, vol. 220, no. 2, pp. 404–426, 2012.
- [169] M. D. Lane and P. R. Christensen, “Thermal infrared emission spectroscopy of anhydrous carbonates,” *J. Geophys. Res.*, vol. 102, no. E11, p. 25581, Nov. 1997.
- [170] J. Michalski, “Silicate alteration mineralogy of the martian surface from TES: Constraints from emission spectroscopy of terrestrial materials.” Ph.D. Dissertation, Ariz. St. Univ, 2005.
- [171] J. M. Palmer and B. G. Grant, *The Art of Radiometry*. Bellingham, WA: SPIE Press, 2009.
- [172] C. Willers, *Electro-Optical System Analysis and Design: A Radiometry Perspective*. Society of Photo-Optical Instrumentation Engineers, 2013.
- [173] J. A. Conant and M. A. LeCompte, “Signature Prediction and Modeling,” in *Infrared Electro-Optical Syst. Handbook, Vol. 4*, M. C. Dudzik, Ed. Bellingham, WA: SPIE Press & Environmental Research Institute of Michigan, 1993, ch. 6.
- [174] M. Ashikhmin and P. Shirley, “An Anisotropic Phong BRDF Model,” *J. Graph. Tools*, vol. 5, no. 2, pp. 25–32, Jan. 2000.

- [175] B. P. Sandford and D. C. Robertson, "Infrared Reflectance Properties of Aircraft Paints," Philips Laboratory, Geophysics Directorate, Tech. Rep., 1994.
- [176] R. G. Priest and T. a. Germer, "Polarimetric BRDF in the Microfacet Model: Theory and Measurements," in *Proc. 2000 Mil. Sens. Symp. Spec. Gr. Passiv. Sensors*, vol. 1, 2002, pp. 169–181.
- [177] K. Caillault, S. Fauqueux, C. Bourlier, and P. Simoneau, "Infrared multiscale sea surface modeling," in *Proc SPIE 6360*, C. R. Bostater, Jr., X. Neyt, S. P. Mertikas, and M. Vélez-Reyes, Eds., Sep. 2006, pp. 636 006–636 006–11.
- [178] J. R. Maxwell, J. Beard, S. Weiner, D. Ladd, and S. Lass, "Bidirectional Reflectance Model Validation and Utilization," Air Force Avionics Laboratory, AFAL-TR-73-303, Tech. Rep., 1973.
- [179] K. E. Torrance and E. M. Sparrow, "Theory for Off-Specular Reflection From Roughened Surfaces," *J. Opt. Soc. Am.*, vol. 57, no. 9, p. 1105, Sep. 1967.
- [180] R. L. Cook and K. E. Torrance, "A Reflectance Model for Computer Graphics," *ACM Trans. Graph.*, vol. 1, no. 1, pp. 7–24, Jan. 1982.
- [181] W. C. Snyder and Z. Wan, "BRDF models to predict spectral reflectance and emissivity in the thermal infrared," *IEEE Trans. Geosci. Remote Sens.*, vol. 36, no. 1, pp. 214–225, 1998.
- [182] J. Krč, M. Zeman, O. Kluth, F. Smole, and M. Topič, "Effect of surface roughness of ZnO:Al films on light scattering in hydrogenated amorphous silicon solar cells," *Thin Solid Films*, vol. 426, no. 1-2, pp. 296–304, Feb. 2003.
- [183] J. Naranen, S. Kaasalainen, J. Peltoniemi, S. Heikkilä, M. Granvik, and V. Saarinen, "Laboratory photometry of planetary regolith analogs. II. Surface roughness and extremes of packing density," *Astron. Astrophys.*, vol. 426, no. 3, pp. 1103–1109, Nov. 2004.
- [184] Y. Shkuratov, A. Ovcharenko, and E. Zubko, "The Opposition Effect and Negative Polarization of Structural Analogs for Planetary Regoliths," *Icarus*, vol. 159, no. 2, pp. 396–416, 2002.
- [185] J. D. Suter, B. Bernacki, and M. C. Phillips, "Spectral and angular dependence of mid-infrared diffuse scattering from explosives residues for standoff detection using external cavity quantum cascade lasers," *Appl. Phys. B*, vol. 108, no. 4, pp. 965–974, 2012.
- [186] S. Sandmeier and K. Itten, "A field goniometer system (FIGOS) for acquisition of hyperspectral BRDF data," *IEEE Trans. Geosci. Remote Sens.*, vol. 37, no. 2, pp. 978–986, Mar. 1999.
- [187] E. Puttonen, J. Suomalainen, T. Hakala, and J. Peltoniemi, "Measurement of reflectance properties of asphalt surfaces and their usability as reference targets for aerial photos," *IEEE Trans. Geosci. Remote Sens.*, vol. 47, no. 7, pp. 2330–2339, 2009.
- [188] C. M. Bachmann, W. Philpot, A. Abelev, and D. Korwan, "Phase angle dependence of sand density observable in hyperspectral reflectance," *Remote Sens. Environ.*, vol. 150, pp. 53–65, Jul. 2014.
- [189] T. H. Painter, "Measurements of the hemispherical-directional reflectance of snow at fine spectral and angular resolution," *J. Geophys. Res.*, vol. 109, no. D18, p. D18115, 2004.
- [190] C. J. Deloye, M. S. West, and J. M. Grossmann, "Changes in apparent emissivity as a function of viewing geometry," in *Proc SPIE 8040*, G. C. Gilbreath and C. T. Hawley, Eds., May 2011, pp. 80 400J–80 400J–12.
- [191] N. A. Macleod, F. Molero, and D. Weidmann, "Broadband standoff detection of large molecules by mid-infrared active coherent laser spectrometry," *Opt. Express*, vol. 23, no. 2, p. 912, 2015.
- [192] C. A. Ortega-Zuñiga, N. Y. Galán-Freyte, J. R. Castro-Suarez, J. Aparicio-Bolaño, L. C. Pacheco-Londoño, and S. P. Hernández-Rivera, "Dependence of detection limits on angular alignment, substrate type and surface concentration in active mode standoff IR," in *Proc. SPIE*, vol. 8734, 2013, p. 87340R.

- [193] A. Banas, K. Banas, M. Bahou, H. Moser, L. Wen, P. Yang, Z. Li, M. Cholewa, S. Lim, and C. Lim, "Post-blast detection of traces of explosives by means of Fourier transform infrared spectroscopy," *Vib. Spectrosc.*, vol. 51, no. 2, pp. 168–176, Nov. 2009.
- [194] B. E. Bernacki and N. Hô, "Differential spectroscopic imaging of particulate explosives residue," in *Proc. SPIE 6945*, C. S. Halvorson, D. Lehrfeld, and T. T. Saito, Eds., Apr. 2008, pp. 694 517–694 517–8.
- [195] X. Liu, C. W. Van Neste, M. Gupta, Y. Y. Tsui, S. Kim, and T. Thundat, "Standoff reflectionabsorption spectra of surface adsorbed explosives measured with pulsed quantum cascade lasers," *Sensors Actuators B Chem.*, vol. 191, pp. 450–456, Feb. 2014.
- [196] D. T. Reid, Z. Zhang, and C. R. Howle, "Active FTIR-based standoff detection in the 3-4 micron region using broadband femtosecond optical parametric oscillators," in *Proc. SPIE*, vol. 9073, 2014, p. 907302.
- [197] F. Fuchs, S. Hugger, M. Kinzer, R. Aidam, W. Bronner, R. Losch, Q. Yang, K. Degreif, and F. Schnurer, "Imaging standoff detection of explosives using widely tunable midinfrared quantum cascade lasers," *Opt. Eng.*, vol. 49, no. 11, p. 111127, 2010.
- [198] P. H. Berning, "Theory and Calculations of Optical Thin Films," in *Phys. Thin Film.*, G. Haas, Ed. Academic Press, 1963, pp. 69–121.